ABSTRACT

Title of dissertation: MOISTURE IN MULTILAYER CERAMIC
CAPACITORS
Daniel Noel Donahoe, Doctor of Philosophy, 2005

Dissertation directed by: Professor Michael G. Pecht
Department of Mechanical Engineering

When both precious metal electrode and base metal electrode (BME) capacitors were subjected to autoclave (120 ºC/100 % RH) testing, it was found that the precious metal capacitors aged according to a well known aging mechanism (less than 3 % from their starting values), but the BME capacitors degraded to below the -30% criterion at 500 hours of exposure. The reasons for this new failure mechanism are complex, and there were two theories that were hypothesized. The first was that there could be oxidation or corrosion of the nickel plates. The other hypothesis was that the loss of capacitance was due to molecular changes in the barium titanate. This thesis presents the evaluation of these hypotheses and the physics of the degradation mechanism. It is concluded by proof by elimination that there are molecular changes in the barium titanate. Furthermore, the continuous reduction in capacitor size makes the newer base metal electrode capacitors more vulnerable to moisture degradation than the older generation precious metal capacitors. In addition, standard humidity life testing, such as JESD-22 THB and HAST, will likely not uncover this problem. Therefore, poor reliability due to degradation of base metal electrode multilayer ceramic capacitors may catch manufacturers and consumers by surprise.

MOISTURE IN MULTILAYER CERAMIC CAPACITORS

by

Daniel Noel Donahoe

Dissertation submitted to the Faculty of the Graduate School of the
University of Maryland, College Park in partial fulfillment
of the requirements for the degree of
Doctor of Philosophy
2005

Advisory Committee:

       Professor Michael G. Pecht, Chair
       Professor Donald B. Barker
       Associate Research Scientist Sanka Ganesan
       Associate Professor Isabel K. Lloyd
       Associate Professor Patrick McCluskey

ACKNOWLEDGEMENTS

TABLE OF CONTENTS

LIST OF TABLES

LIST OF FIGURES

Chapter 1:   INTRODUCTION

Advances in electronic products and technology brought about by semiconductor development have mesmerized public attention for the last two decades. Moore's Law[1] has helped people grasp the blistering pace of semiconductor evolution. However, the growth of semiconductor technology has rested on the shoulders of less glamorous passive components[2]. As progress along the curve established by Moore's Law resulted in integration of more functionality onto each integrated circuit, fewer ICs on each printed wiring board were required. At the same time, the trends toward lower IC voltages and to higher digital operating frequency require more passives to maintain signal integrity. As a result, the relative ratio of semiconductor parts to passive parts has grown heavily in favor of passives. For example, approximately 90% of the components on a cell phone are passive components. Approximately 60% of the cell phone passive components are capacitors[3], and most of the capacitors are multilayer ceramic capacitors[4] (MLCC). This example shows that the MLCC has quietly become the dominant component type in digital electronics.

Just as semiconductor technology once held the limelight, the latest technical craze is nanotechnology.   By historical accident, the capacitor was the first nanotechnology based electrical component. During World War II, ceramic capacitors were made from imported mica, but the sea lanes were not secure.   Wartime efforts

---

[1] Moore's Law states that the transistor density on an integrated circuit doubles every 18 months.
[2] Passive components include resistors, inductors and capacitors.
[3] A capacitor, in its simplest configuration, is a dielectric, a nonconducting material, separating two electrodes. A capacitor stores charge and acts as a filter to remove noise.
[4] The MLCC is a rectangular sintered component with solderable ends. MLCCs are made up of a sandwich of as many as several hundred sub 2 micron electrodes. The ends are terminations that attach to the electrode halves.

resulted in the invention of capacitors based on sintered[5] barium titanate ($BaTiO_3$) as the dielectric [26] [46]. It was 1941, and no one knew how profound this invention would turn out to be in the future.

The crystalline barium titanate molecule (called the unit cell in crystallography) has a unique physical structure. Barium titanate belongs to a class of minerals called perovskites. The generalized chemical structure of perovskite is ABO_3 where A and B are cations, a variety of elements. The archetype perovskite is $CaTiO_3$; perovskite thought to be the most common mineral in the earth's mantle [48]. Barium titanate goes through 4 solid phase changes, but it is the tetragonal[6] phase existing between 0 °C and 130 °C that is useful for capacitors. In the tetragonal phase of barium titanate, the titanium atom sits in the middle of a rectangular box formed by barium atoms in the corners and oxygen atoms in the rectangular faces. The titanium atom is offset from the center of the rectangle by just over 1% of a nanometer. The magic is that this titanium atom can spontaneously move up or down, into two positions like an open or closed door. By applying a voltage, many of these atoms move together, storing charge. As described, pure barium titanate makes a great capacitor, but nature provided even more benefits, opportunities that are still being exploited. Atoms of other elements can be mixed with barium titanate to form what is descriptively called a solid solution. If the right elements are mixed in the correct ratios, capacitive properties can be modified to perform better across a temperature range or to make a high value capacitor at one temperature. A great

---

[5] Sintering is the combination of processes which bond a fine molded ceramic powder into a dense solid by heating. The goal of sintering is to reduce pores to create a dense material. The driving force during sintering is the overall reduction in surface energy. Atomic mechanisms lead to coarsening and densification. Sintering can be either by solid state or liquid phase sintering. [78].

[6] Tetragonal is one of the 7 basic crystal systems; it has 90° angles and two sides equal.

many patents have been granted with various methods of assembling capacitors, various sintering processes and varieties of mixing of barium titanate and additives. These additives (some for the A and some for the B perovskite sites) include, but are not limited to, calcium, cerium, cobalt, dysprosium, erbium, hafnium, holmium, lead, lithium, magnesium, niobium, silicon, strontium, tin, uranium, vanadium, yttrium, ytterbium and zirconium.

Since World War II, industry has taken the MLCC through several design iterations. The industry developed accepted industry-wide standards defining MLCC sizes and performance testing. In general, the most temperature-stable dielectrics (EIA designation COG[7]) have the lowest capacitance for a given component case size. The dielectrics that offer the most variable capacitances (variable meaning capacitance values change across temperature) also provide the highest capacitance values (EIA designation Y5V). An effect called dielectric aging (capacitance decreases over time just sitting at room temperature, by as much as 7% per decade hour for the Y5V dielectric[8]) is described in the standard. Although the capacitor industry has used alternative perovskites called lead relaxors[9]; the primary MLCC dielectric choice (up until recently) has become modified barium titanate sintered in air. The electrodes and terminations began as silver and settled on a mix of palladium and silver in order to get the melting temperature compatible with the sintering temperature of barium titanate. The palladium silver electrode configuration is also called precious metal electrodes (PME). The

---

[7] The many Electronic Industries Association ceramic dielectrics are defined in EIA-198 [2].
[8] The capacitance degrades up to 7% in 10 hours, 21% in 1000 hours (42 days), 28% in 10,000 hours (1.2 years) or 35% in 100,000 hours (12 years). Aging can be reversed by heating above a value called the Curie point (130 °C for pure barium titanate and customarily taken as 125 °C for multilayer capacitors).

sintering temperature of barium titanate is optimized differently by each MLCC producer; the vendor specific sintering temperature range begins at 1100 °C and goes up to at least 1500 °C (Barium titanate does not melt until 1715 ºC.). The melting temperature of silver falls at only 962 °C; the melting temperature of palladium is 1555 °C. Since palladium is more expensive than silver (historically more than 10 times more expensive), the industry used a mix ratio of in favor of silver (typically 30% palladium and 70% silver). However, there has been a big change underway over the last few years.

After the Cold War ended, an end defined by the fall of the Berlin Wall in 1989, there was an unanticipated effect on the MLCC producing industry. Russia provides over 50% of the world's annual production of palladium; the largest alternative source is South Africa at 33%. Political instabilities after the end of communist rule in Russia resulted in suspension of Russian palladium shipments in 1997. The price of palladium rocketed from 125 USD per troy ounce[10] to almost 1100 USD per troy ounce (approximately four times the price of gold at the time). Although the automotive industry uses the lion's share of worldwide palladium production for catalytic converters, the palladium demand from the electronics industry was primarily for palladium in capacitors.

The capacitor industry responded to the palladium price pressure by pulling out an old trick. Industry researchers around the world had been working on so-called base metal electrodes for a long time. U.S. patent literature first provides details of base

---

[9] Relaxor refers to a perovskites structure with an ordering of the B site cations that requires eight perovskites units to form a unit cell. These are also called "complex" perovskites [44].

[10] USD is United States dollars. A troy ounce is equal to 0.031 kg.

metals[11] for capacitor electrodes filed in 1952. The patent by Herbert and Best (granted in 1956) described a set of base metal electrode candidates that included nickel, tantalum, iron, cobalt, chromium, manganese, columbium and vanadium [61]. Nickel has become the preferred choice. The reason that the industry had not moved to base metal sooner was that firing in air would destroy the electrode by oxidation. Solving this problem by removing oxygen from the firing atmosphere by adding nitrogen or inert gas causes another problem, degradation of the barium titanate through the chemical process of reduction (removal of oxygen). This reduction problem was solved by additives and by careful control of the firing atmosphere[12]. Base metal electrode capacitors first entered the market around 1990. Large scale production change in the industry to base metal electrode capacitors began in 1998 (corresponding to palladium prices). Now, unless military grade capacitors are ordered, deliveries of MLCCs will probably be base metal electrode (BME) parts [49] [50].

Original equipment manufacturers (OEMs) and MLCC producers have long focused on the reliability of MLCCs, because MLCCs are such an integral part of electronic products. The industry has developed standard tests for reliability. These tests are based on exposure to accelerated environments for specified periods of time followed by a pass-fail criterion. There are 4 primary standard reliability tests, the type of test sometimes referred to as highly accelerated stress tests (HAST) [1]. These tests can be summarized as (1) a moisture resistance test for 500 hours at 40 ˚C and 95% relative

---

[11] Base metals are metals other than the noble metals (such as silver and palladium).
[12] Appendix D presents a derivation of the Ellingham Diagram, a diagram providing a representation of the thermodynamics of the oxidation-reduction issue presented by the change to nickel electrodes. The implications of the Ellingham Diagram are further discussed in the appendix. The results of the precarious

humidity (RH) without electrical power, (2) a damp heat for 500 hours at 85 ˚C and 85% RH with electrical power, (3) a life test for 1000 hours at 40 ˚C and 95% at twice rated power and (4) a thermal shock test of 5 unpowered cycles of –55 ˚C to 125 ˚C (reduced to –30 ˚C to 85 ˚C for Y5V). Surviving HAST is thought to guarantee that the capacitor design meets requirements, viz., OEM needs. In addition to these standard capacitor industry tests, many manufacturers also conduct what is called a highly accelerated life test (HALT) during MLCC development. The goal of HALT is to predict the capacitor's life in the field. HALT is based on exposing capacitors to voltages up to 12 times the specified voltage and high temperatures up to 175 ˚C simultaneously. While conducting these tests, reliability engineers always wonder if the tests are really will predict whether the capacitor will meet needs. The only way to maintain confidence in any reliability tests is to continually scrutinize the tests against field results.

Testing for humidity tolerance is especially important for barium titanate capacitors. Barium titanate reacts with moisture; it is hygroscopic. Powdered barium titanate readily dissolves in water (more precisely, the barium leaches away). Since MLCCs are sintered, only the surface atoms are involved in the moisture reaction. Solid state sintered materials typically contain some porosity since it is difficult to densify them to 100% theoretical density via diffusional processes. If small interconnected voids are present, a sintered material will absorb moisture from the atmosphere like a sponge. This is the operational principle of desiccants familiar in packaged shipping bags. In addition, if the interface of the electrode to the dielectric is poor, small voids may form along the

---

balance of ionic species (and vacancies) left in the capacitors after manufacture will be important in Chapter 6.

electrodes. Moisture is also more conductive than the dielectric, providing a current leakage path. Therefore, an MLCC is vulnerable to moisture attack if the capacitor is porous.

This thesis demonstrates a new degradation mechanism for MLCCs due to high relative humidity. Degradation is shown by exposure of a group of MLCCs to accelerated temperature and humidity combinations. The most aggressive condition is called the autoclave (121 °C and 100% RH). Testing also was completed at room temperature with 100% RH and at 85 ºC with 85% RH. Testing focused on (but was not limited to) one size and one dielectric MLCCs with both BME and with silver-palladium electrodes [4]. There are two relevant industry capacitance degradation metrics. First, the standard damp heat test has a passing criterion of a $\pm$30% change in capacitance (at 500 hours) [3]. Secondly, manufacturers specify a capacitor lower tolerance at 1000 hours.

The autoclave test resulted in average values of the BME capacitors degraded from starting capacitances just below the -30% criterion at 500 hours. This is expected since the autoclave condition is more severe. However, the precious metal electrode (PME) capacitors degraded less than 3% from their starting values (within expected maximum of up to 7%). Heating the PME and BME capacitors above their Curie Temperatures (a procedure called de-aging) after approximately 500 hours of autoclave exposure resulted in the PME capacitors returning to their initial values. The BME capacitors did not recover to their original values.

Autoclave testing was continued to over 2500 hours, 5 times the elapsed time in standard damp heat testing. There was a surprising result over this longer time

7

perspective. All the Y5V dielectrics appear to degrade, but not by the logarithmic aging rule. Instead, they appear to degrade by an exponential rule governed by a time constant. The time constant observed for the 0805 size (2 mm by 1 mm) BME MLCCs was about 250 hours, and a much larger time constant for the PME MLCCs was observed[13]. The significance of having a time constant is that it suggests that there may be a chemical reaction underway during the autoclave test, especially evident in the BME capacitor data. This is supported by the fact that baking out after exposure did not reverse BME capacitor degradation. This testing showed that there is a difference between BME and PME capacitors. Testing at the other high humidity conditions provided different time constants, but these tests resulted in similar outcomes.

Analysis of the capacitor began with optical microscopy of epoxy encapsulated and finely polished cross sections. Interesting features were further inspected by higher power magnification using a scanning electron microscopy (SEM). These methods revealed details of the dielectric and its construction. By cutting microscopic stair shaped groves into the dielectric to expose fresh surfaces using a technique called focused ion beam (FIB), physical details of the ceramic to metal interfaces were inspected. Although some interface voids were found, in general the nickel to barium titanate bonding was not porous. BME capacitors use copper terminations made in a second firing operation using a copper paste containing some glass (for bonding the copper termination to the barium titanate dielectric) [52]. There were large voids in the termination, but the voids were not continuous through the termination. Elemental identification was by electron dispersive spectroscopy (EDS). The PME and BME Y5V dielectrics have different elemental

---

[13] A time constant of 8000 hours is discussed in section 5.4.

constituents. Identification of grain crystallographic orientation was by electron backscatter diffraction (EBSD). Inspection of the sintered dielectrics showed that they are made up of many randomly oriented individual crystallites called grains, and the PME and BME grain sizes are different by almost a factor of 3. The differences in grain size and in elemental constituents both reflect the differences in firing temperature.

The observed reduction in capacitance must be due to chemistry occurring inside the capacitor body. The surface of electrodes is inaccessible to easy viewing. The electrodes are buried within a tough ceramic body and are only a couple microns thick. Furthermore, several investigative methods were used to study if moisture was moving into the ceramic body. If moisture, or water's constituent oxygen, were interacting with the capacitor, then a logical reaction site would be at the nickel electrode surfaces. If the electrodes were oxidizing, they should swell (nickel oxide is less dense than pure nickel). Swelling could explain a change in capacitance. X-ray photoelectron spectroscopy (XPS) was used to investigate changes in the electrodes.

Therefore, the story of ceramic electronic devices underpins twentieth century electronics, because electronics exploits the century's advances in solid state physics (solid state physics includes semiconductors, ceramics and nanotechnology). The motivation for bringing concepts from solids state physics into practice always arises out of practical needs. The PME to BME capacitor design change provides just such an example. Practical cost considerations drove technology out of the laboratory and into practice. Despite years of experience, making the swap to from PME to BME seems to have introduced a practical reliability issue.

Capacitors are required to guarantee signal integrity in digital devices such as personal computers and cell phones [27]. To reduce price, the ceramic multilayer capacitor industry has been migrating from precious metal electrodes (PME) made of silver-palladium to base metal electrodes (BME) made of nickel with copper terminations. Although the initial development work on base metal electrodes can be traced back to the early 1960s [19], this transition began to phase into production in 1998 in response to increases in the price of palladium [5]. The transition is progressing quickly. For example, the author placed an order for precious metal capacitors in 2004 only to discover that the parts delivered were, in fact, base metal electrode capacitors. This transition is an issue for military and high reliability applications, because base metal electrode multilayer capacitors are not yet approved to replace military grade precious metal capacitors, MIL-ER [6].

Chapter 2:   TEST BASED SPECIFICATION AND LIFE ESTIMATES

The capacitor industry uses a unique method of specifying the application environment for ceramic multilayer capacitors in product literature. The industry describes their evaluation testing for product compliance with customer lifetime environmental exposure requirements rather than on specifying the field environment. Each firm employs slightly different testing regimens. Some firms use internal testing standards, and others use industry standards such as EIA 198. Tests include aspects unrelated to life. Only those tests related to life will be discussed in this paper. Table 1 provides a summary of typical (compiled from capacitor vendor catalogs) environmental tests related to temperature-humidity exposure with generalized test names and generalized test descriptions. These tests are done with the capacitor soldered to a printed wiring board. In the literature, the load humidity life test has been reported to change capacitance by 10% in an EIA 1210 Y5V 10 µF lead relaxor based capacitor after 2000 hours [14].

Table 1: Temperature-Humidity Tests

Moisture Resistance	Load Humidity	Life Test	Thermal Shock
40 ℃, 95% RH 500 hours, Unpowered	85 ℃, 85% RH 500 (to 1000) hours, 1X Rated Power	125 ℃ to 85 ℃, 0% RH 1000 hours, 2X Rated Power	-55℃ to 125 ℃ (-30℃ to 85 ℃) 5 cycles Unpowered

In addition to the tests described in product literature, the industry customarily predicts capacitor life using highly accelerated life testing (HALT) [7] [8] [29]. This is an accelerated testing strategy based on voltages and temperatures well beyond the test

specifications described in Table 1. The goal of HALT is to accelerate wear out effects and to extrapolate from the accelerated failure rate to the expected failure in field conditions. Average values are generally used at both ends, because it is the expected values, viz. averages, which are of interest. The underlying extrapolation is by means of the acceleration factor by Prokopowicz and Vaskas [9]. Their equation is shown is below.

$$A = \frac{t_1}{t_2} = \left(\frac{V_2}{V_1}\right)^n \exp\left(\frac{E_a}{k}\left(\frac{1}{T_1} - \frac{1}{T_2}\right)\right) \tag{1}$$

In this equation, A is the dimensionless factor describing the acceleration. The subscript 1 refers to the accelerated temperature and voltage. The subscript 2 refers to the intended field condition. The constant k is the familiar Boltzmann's constant, 8.62E-5 eV/K. The exponent n is empirically determined, and it typically ranges from 3 to 7 depending on the dielectric strength of the dielectric layer. The constant E_a is the thermal activation energy representing dielectric wear out that might be described in terms of the bathtub curve [9]. The underlying mechanisms are due to migration, probably assisted by intrinsic ionic processes [12].

Randall et al. [7] used HALT for a X5R[14] dielectric class part. They reported using a voltage ratio of 8 and a maximum temperature of 140 ºC. Randall et al used an order of magnitude change in insulation resistance as their failure criterion. Paulsen and Reed [8] reported using a voltage ratio of 12 and temperatures as high as 175 ºC. Paulsen et al used a leakage current threshold of 100 µA as the failure criterion. Randall et al. suggested that Prokopowicz and Vaskas equation should be modified by another

multiplier for capacitor area. Another weakness of this expression is reliance on only temperature and voltage as accelerating factors.

Environmental tests are often accomplished by following a generic testing method such as the environmental testing described in standards such as IEC 68-2 [3] and IEC 60749-33 [4]. Commercially available test equipment is readily available to create these environments.

Test results presented in this thesis indicate that widely used tests shown Table 1 and HALT may be insufficient to demonstrate the suitability of the new BME capacitors for some humid environments. In addition, barium titanate has been reported to leach in water at initial rates of 1.1 µg/m^{2}s at 25 ˚C increasing to 4.0 µg/m^{2}s at 100 ˚C [23]. Utech described the chemistry of the dissolution process [25].

---

[14] EIA 198 specifies the X5R as a class II dielectric with a temperature characteristic over the range of –55 ºC to 85 ºC of $\pm$15%. This dielectric is compared to others in Table 2. The capacitor tolerance is a distinct performance parameter from its temperature characteristic.

Chapter 3:   AGING OF BARIUM TITANATE CERAMIC CAPACITORS

Multilayer ceramic capacitors suffer a loss of capacitance over time, an effect separate from the lifetime described in relation in equation (1) for HALT. This effect is called aging, and it is an effective decrease in the dielectric constant. Aging is described by the following equation (2) where the values of k, the dielectric aging rate, are listed for some common dielectric types in Table 2. The Y5V is commonly used as a bypass capacitor[15]. The X5R and X7R dielectrics are often used as decoupling capacitors[16]. The Y5V dielectric is popular in low price electronics [21].

The initial capacitance is C_o. Of course, equation (2) is only an industry-accepted approximation of what really occurs. For example, the common logarithm becomes zero when time equals 1, negative for time less than 1 and infinite at time zero. None of these values makes any sense, but the value of aging at these small durations is not of practical industrial interest. Equation (2) would predict a negative capacitance for Y5V MLCCs for times greater than 22 billion years. This long term prediction of aging is not reasonable either, because 22 billion years is not a reasonable MLCC lifetime. Since the logarithmic equation describes an aging process that is rapid in the first few hours, the industry uses a reference point for the performance of capacitors at 1000 hours of age from the time of last heat, TOLH [13]. At Y5V's 7% maximum aging value, the initial

---

[15] A bypass is a parallel path for high frequency current to flow around a component in a circuit. A bypass provides steady direct current to the component [83].
[16] A printed wiring board with high speed digital components uses decoupling capacitors between the power and ground pins to reduce voltage sag (i.e., degraded signal integrity) and radiated emissions. The capacitors act as local sources of charge during switching, and MLCCs perform this function better than other capacitor types [84].

value, Co, must start at 27% above the nominal value in order for the 1000 hour value to fall on the nominal.

$$\frac{C}{C_o} = 1 - k \log t \qquad (2)$$

Aging is a gradual process in dielectrics made of barium titanate. It begins after the capacitor's last excursion beyond the Curie point. The Curie point for pure barium titanate is between 120 and 130 ºC[17], and the dielectric constant changes between 120 ˚C and 130 ˚C [16][24]. The Curie point can be adjusted by doping the barium titanate dielectric, and the actual point is shifted in most capacitors. Capacitors can be restored to their original capacitance by heating them above their Curie point for period of time. This process is called "de-aging." Various MLCC vendors recommend de-aging by holding 125 ºC for four hours or 150 ºC for one hour, although another vendor claims one half hour is adequate.

Table 2: Dielectrics (EIA 198)

EIA Dielectric	Dielectric Class	Low Temperature Rating [ºC]	High Temperature Rating [ºC]	Maximum Temperature Shift	Maximum % Capacitance Loss/Decade Hour
C0G	I	-55	125	$\pm$ 30 ppm/ºC	0
X5R	II	-55	85	$\pm$15%	2
X7R	II	-55	125	$\pm$15%	2.5
Y5V	III`	-30	85	+22% -82%	7

The barium titanate dielectric in multilayer ceramic capacitors is polycrystalline. The relief of the mechanical stress locked into the structure during the phase change from

---

[17] Multilayer capacitor manufacturers modify the dielectric properties to obtain the best properties. For example, adding lead or strontium adjusts the Curie point up or down (respectively).

cubic to tetragonal plays a role in aging. Aging is thought to be due to thermally assisted domain boundary migration [18]. Brandt and Ansell reported dielectric constant aging measurements for polycrystalline barium titanate. Putting their reported values into the units of k, they report k = 2.7 at 30 ℃ increasing to 3.4 at 90 ℃ [10].

Chapter 4: CAPACITOR INSPECTION AND ANALYSIS

Samples of commercial capacitors from Kemet, Murata and TDK were selected for humidity testing. Two of the BME multilayer ceramic capacitors are 1 µF capacitance, Y5V dielectric, 16 Volt, 0805 size (2 mm by 1 mm) with tolerances of -20% to +80%. A Kemet with 0.1µF capacitance, Y5V dielectric, 25 Volt, 0805 size was selected for the precious metal multilayer ceramic capacitor. Also 1812 X7R BME were tested. These parts were selected on the basis of what was available from the distributor. The minor differences in capacitances and voltages between these capacitors should be important in interpreting the results of testing. All of these capacitor manufacturers produce high quality products, and no product defects with these brands were uncovered in the course of this thesis study.

4.1: Cleaved MLCC Cross Sections

In addition to encapsulated and polished cross sections, capacitor samples were mechanically split in half using a custom tool with positioning rails and hardened steel faces (Figure 1), optically inspected and inspected by SEM to check for any aberrations from the effects of polishing. Energy dispersive x-ray spectroscopy (EDS) data was also created for the cross sections to determine the elemental composition of the capacitors. However, EDS can not resolve most of the low level impurities and modifiers in capacitors. Description of the constituents of BME capacitors is provided in U.S. patents [63] [64] (Philips Corporation, sold their patent to DMC2 Electronic Materials in 2001).
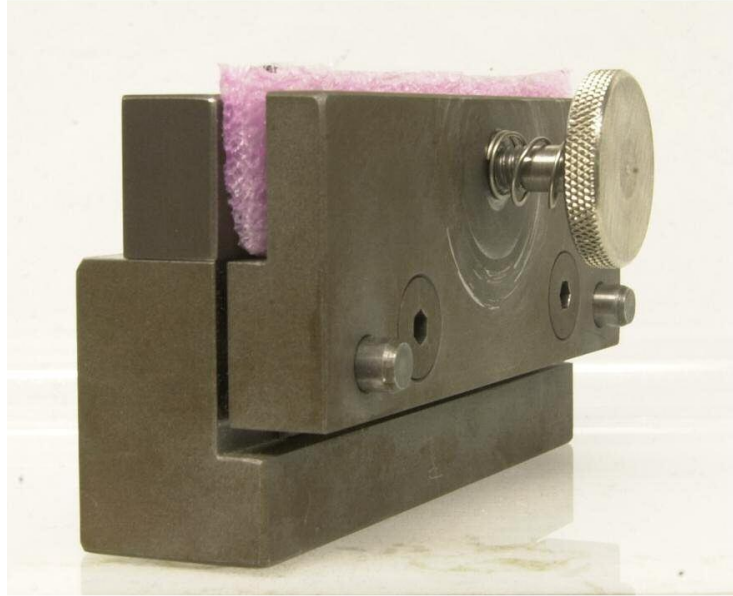
Figure 1: MLCC Cleaving Tool

4.2: Nondestructive Inspection Method to Distinguish MLCCs by Electrode Type

One of the issues in the transition from precious metal electrodes to base metal electrodes is the practical matter of telling one from the other. There is no visual distinguishing feature whether a MLCC is made with BME or PME. Therefore, a nondestructive method to differentiate the two types of capacitors was invented. Since nickel is magnetic and neither palladium nor silver are magnetic, a magnetized steel probe of the right size was selected and, upon approach to the body center of the capacitor, would cause the BME style to move. The precious metal capacitor would not move. A patent application was filed to explain and extend the concept to high volume production [47]. This same magnetic concept was used with cleaved capacitors by approaching the nickel electrode face. This method proved useful. When a reel of PME parts was ordered during the thesis investigation, BME parts were delivered. This is despite that fact that the distributor and the factory were specifically told that the PME

version as described in the vendor catalog were desired and the order form was made out as the distributor suggested. Therefore, this is evidence that the MLCC part supply chain has converted commercial MLCCs to BME without attention to the electrode type.

4.3: Encapsulated Section Inspection

Epoxy encapsulated cross sections of samples for each of the capacitor types were made for inspection. After polishing, both optical and scanning electronic microscope (SEM) images of the lapped and polished encapsulated cross sections were collected. Descriptive parameters for the capacitors are provided in Table 3.

Table 3: Capacitor Parameters

Vendor	Electrode Material	Initial Average Capacitance [nF]	Dielectric	Primary Dielectric Elemental Constituents (non-BaTiO$_3$)	Electrode Elemental Constituents	Dielectric Thickness (µm)
Kemet	BME	881	Y5V	Ca, Zr	Ni	9.9
Murata	BME	1154	Y5V	Ca, Zr	Ni	7
Kemet	PME	94	Y5V	Ca, Pb, Zr	Ag, Pd	13
TDK	BME	102	X7R	Y	Ni	46

Initial inspection efforts focused on the interface of the termination to the dielectric. For example, figure 2 is an optical image of cross section of a Kemet BME 1 µF MLCC (This capacitor has 65, 2 micron thick electrodes.). The work began with the hypothesis that moisture might be finding a path along the termination to dielectric interface. For example, an AVX reference [30] suggested that moisture migration through connected pores could be an explanation for humidity degradation of MLCCs. Other researchers had also studied problems caused by the migration of silver from electrodes or terminations in MLCCs [79]. Therefore, as inspection was underway, it was expanded to also look at voiding along the electrode to dielectric interfaces. Unfortunately,

interfaces are usually damaged by lapping and polishing the cross sections, and AVX Corporation suggests filling the epoxy encapsulant with zirconia. Rather than pursue modified potting methods, the Focused Ion Beam (FIB) offered a better alternative The FIB can precisely mill into the capacitor body for inspection below the disturbed surface.

0.3 mm
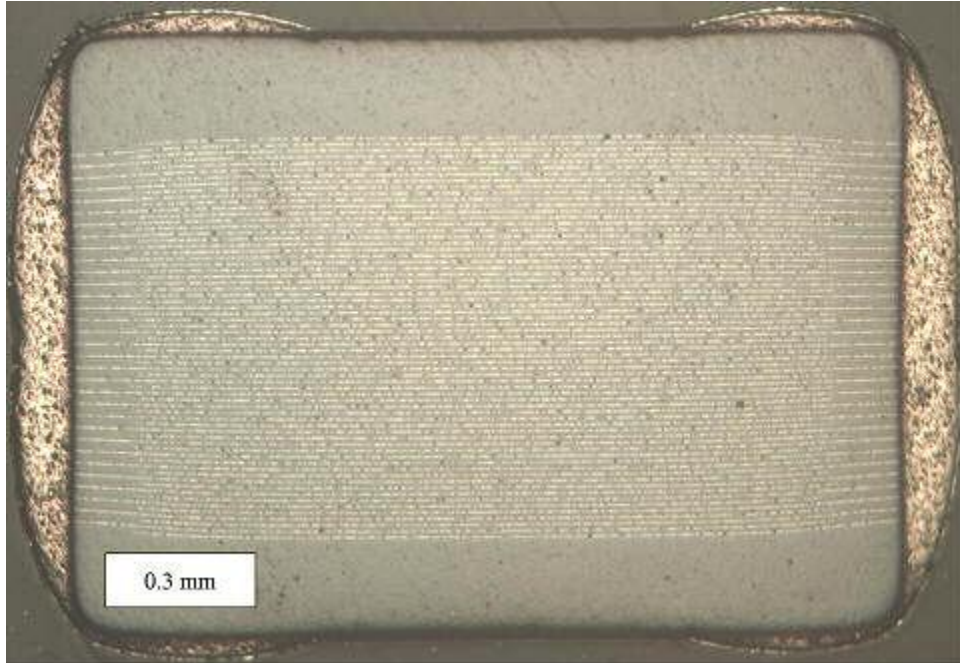
Figure 2: Kemet 0805 BME MLCC Cross Section

Figure 3 shows an image of the same part number with two sections milled out by the focused ion beam[18]. The milling is done is a stair step pattern that can be seen in the image in order to get better images of the termination interface without inadvertent damage due to lapping and polishing. Figure 4 shows an SEM image of the smaller milled out section. The smaller section (on the right) is approximately 10 by 14 microns in area. The image shows a number of fascinating features of the interface. The features include apparent crystalline structures in the dielectric probably caused by the

---

[18] FIB work done by Mr. John Barry using the FEI-620 Dual Beam SEM/FIB in Professor Jon H. Orloff's Laboratory for Ion Beam Research and Applications (LIBRA) at the University of Maryland.

temperature excursions at the application of the copper terminations. However, the shiny copper in this image appears to be voids. Although the FIB images provided additional insight into the physical construction of the MLCCs, the FIB images did not completely answer the question of whether there were voids at the interface. Therefore, another method was used.
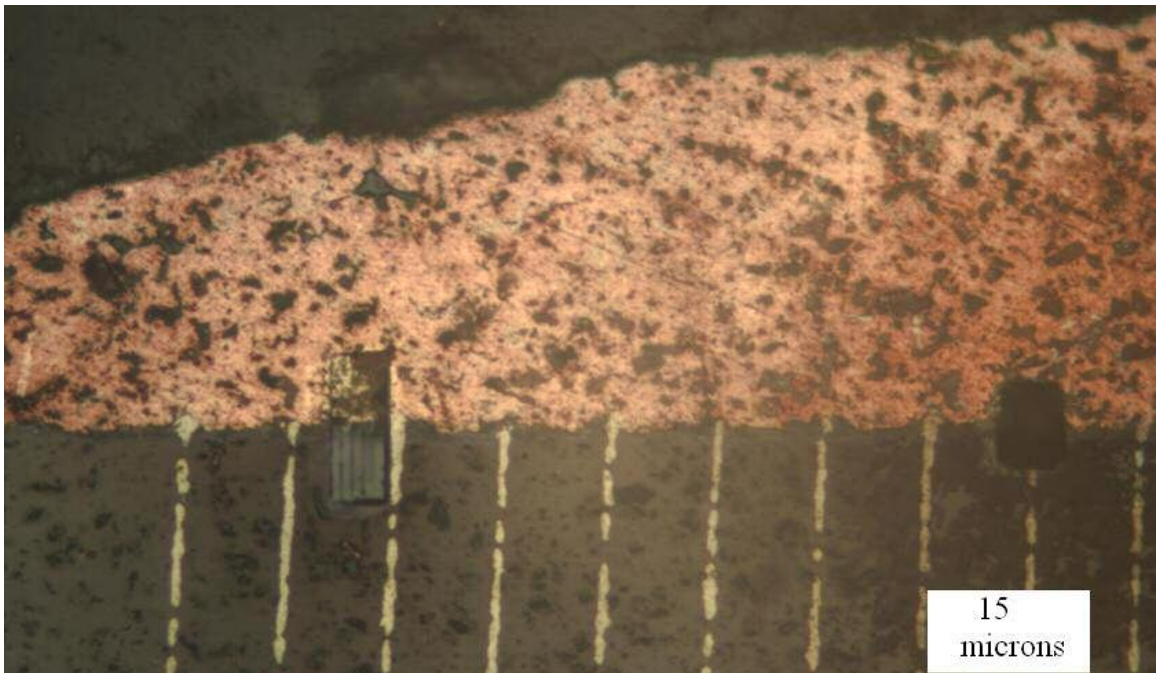
Figure 3: Optical image of Kemet BME at Termination to Dielectric Interface Showing FIB Cuts
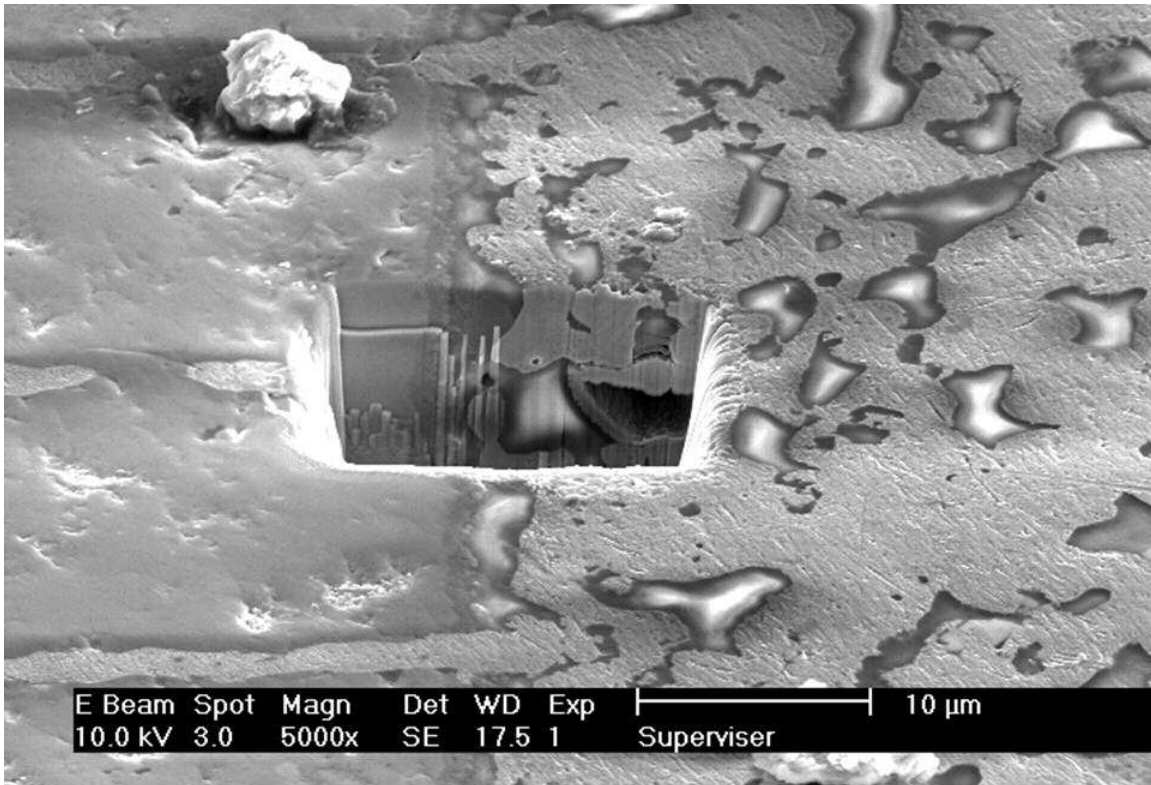
Figure 4: SEM of Kemet BME Section after FIB at Termination Interface

Electron Backscatter Diffraction (EBSD) in the SEM is a method (introduced commercially in 1994) that can functionally substitute for Transmission Electron Microscope (TEM) and x-ray diffraction (XRD) techniques. EBSD provides detailed crystallographic information. The software is called Orientation Imaging Microscopy (OIM™) and is provided by EDAX Inc. Figures 5 through 8 provide EBSD analysis data for the Kemet BME.

Figure 5 is an EBSD orientation image of three electrodes at the interface to the copper termination. EBSD images are sensitive to surface imperfections in a manner similar to optical images described above, and the fine grain appearance along the interface of the copper to dielectric is not a real phenomenon. Figure 5 includes all three

phases, copper, nickel and barium titanate. The legend shows grain orientation in terms of crystalline directions. Pole figure representation is explained in Appendix A. Figure 6 separates the three phases for clarity. The nickel electrode is only one grain across. There are approximately 12 barium titanate grains between the electrodes. Figure 7 shows that the dielectric average grain size is just under 2 microns. Barium titanate filled into some of the adjacent apparent voids in the copper termination. Figure 8 is the pole diagram for the dielectric phase in units of times random (see the appendix), and the maximum value of under 2.9 indicates a random distribution.

Figure 9 contains two EBSD images[19], an Electron Dispersive Spectroscopy (EDS) image and an image quality map. The image quality on the right serves two purposes. First, it shows that structure being analyzed by EDS. Secondly, the image quality map shows good resolution in light colors and poor resolution in darker colors. The image depicts the interface issue discussed in the previous paragraph. The EDS image on the left reveals diffusion of copper from the termination into the nickel electrode. The copper content diminishes with length as would be expected. The driving temperature is applied during termination attach. This diffusion detail is not resolved by the CALCE[20] ESEM™. The EBSD image is clear in soft copies, but the fine shades will not be as evident in gray scale printouts. The understanding provided by further spectroscopy may return to involve this observation.

Similar EBSD analysis was undertaken for a PME MLCC. One question was whether there was any migration of the silver into the dielectric. Migration (if only into

---

[19] EBSD analyses were performed at EBSD Analytical Inc. of Draper, Utah.
[20] University of Maryland CALCE, Electronic Products and Systems Center

adjacent dielectric grains) might explain how the PME could be sealing off a moisture flow path that could be present in the BME MLCCs. However, careful EBSD analysis showed no migration of the electrode into the dielectric.
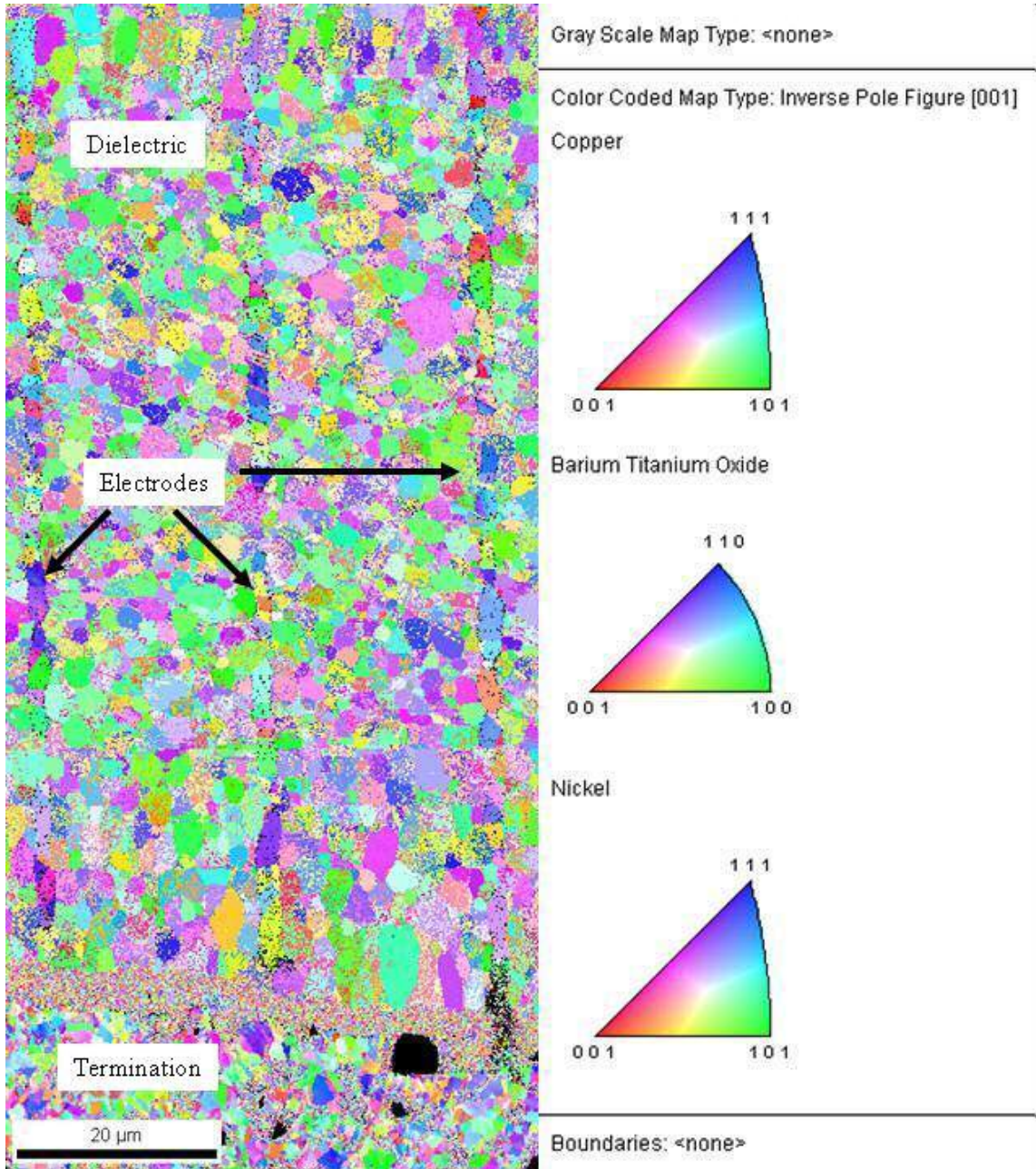
Figure 5: Electronic Backscatter Diffraction (EBSD) Image of Kemet BME MLCC
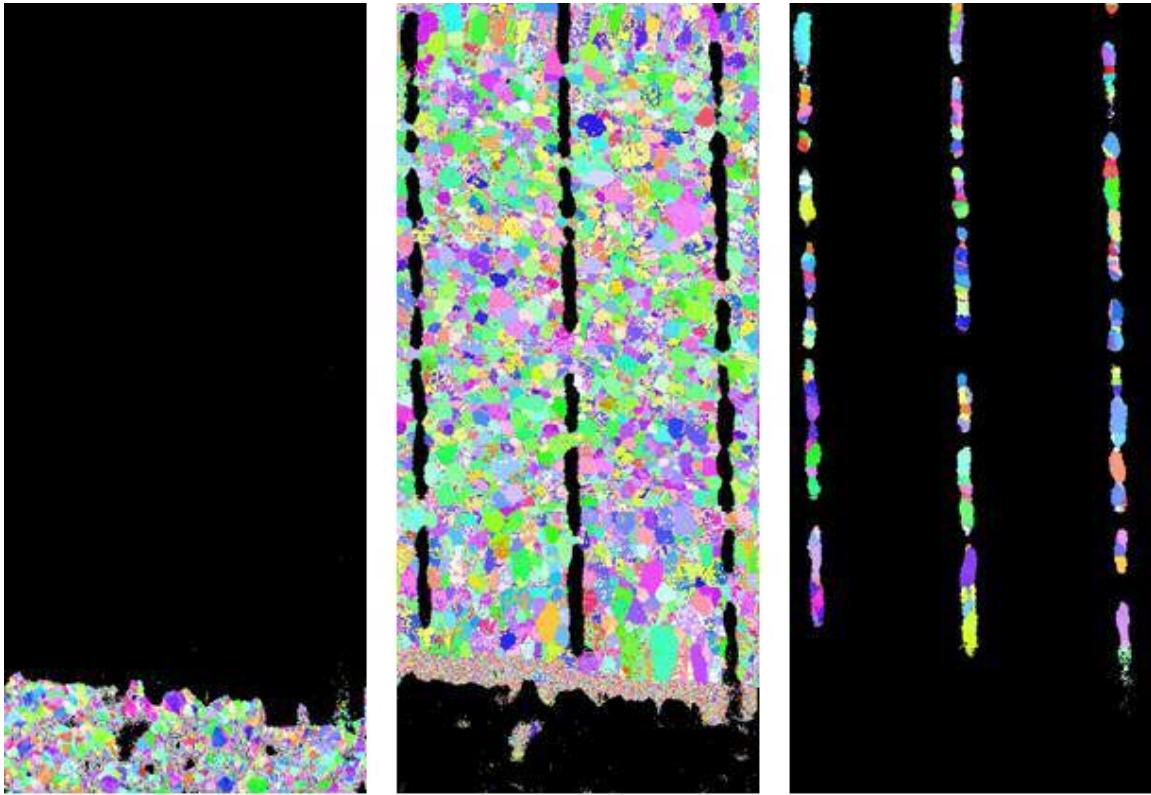
Figure 6: Kemet BME MLCC EBSD Images with Phases Separated
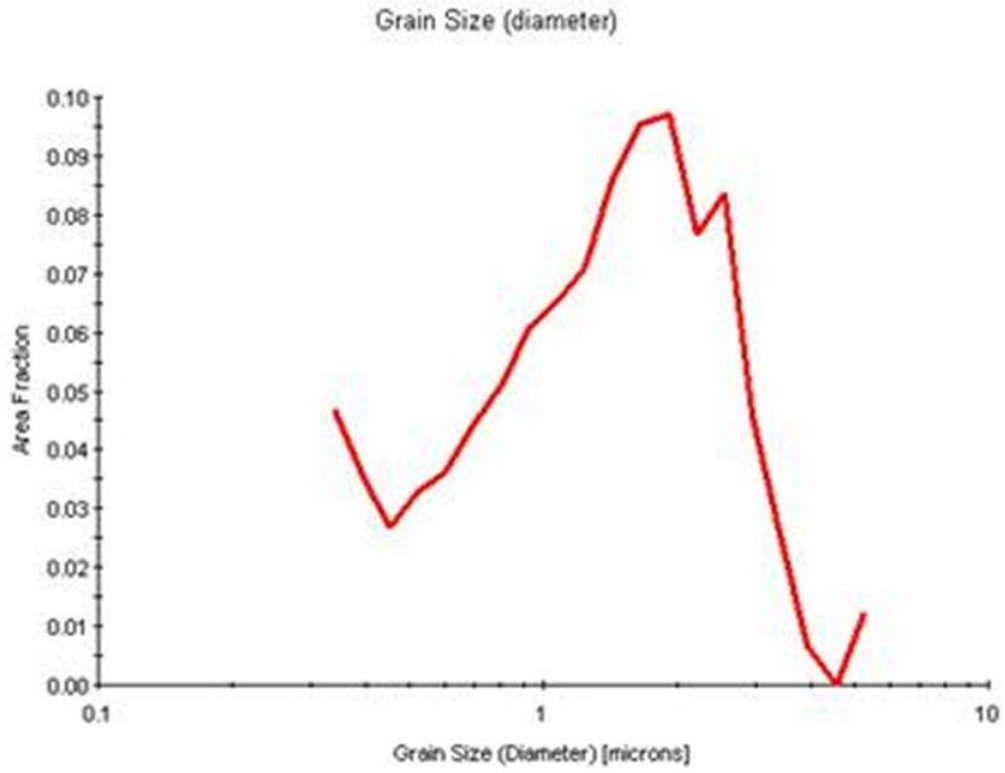
Figure 7: Kemet BME MLCC Dielectric Grain Size Distribution
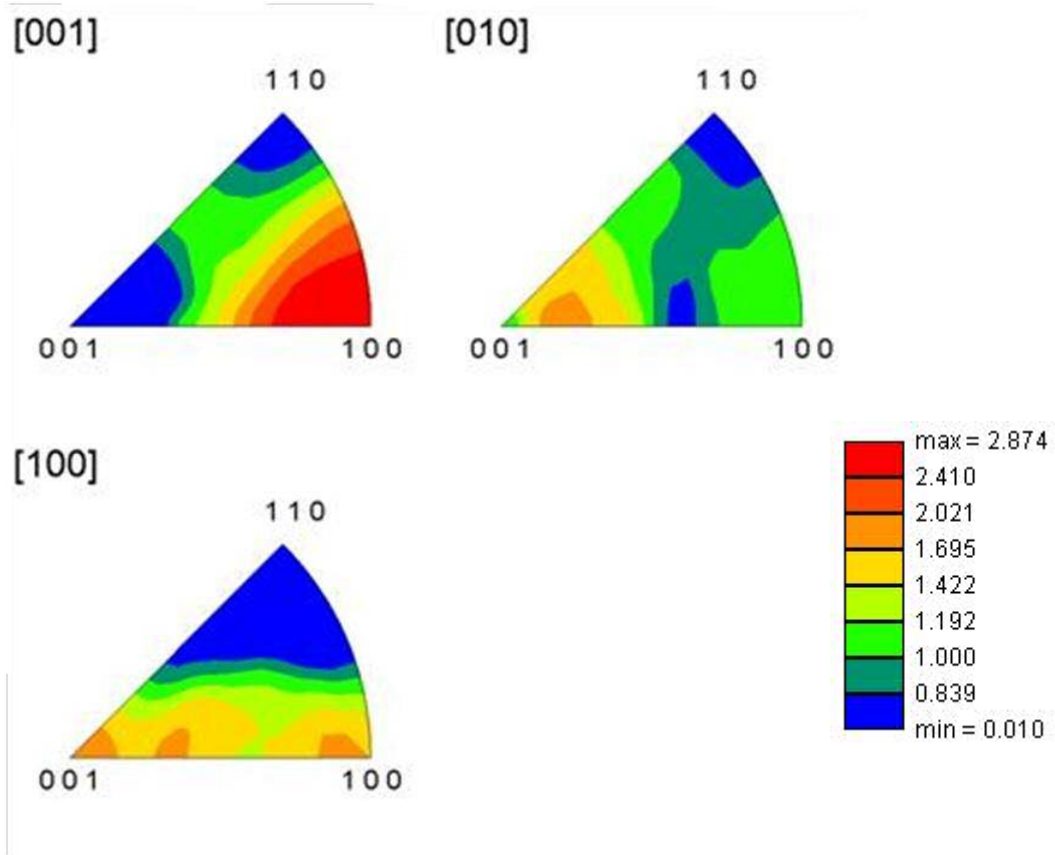
Figure 8: Inverse Pole Diagram for Kemet BME MLCC Dielectric
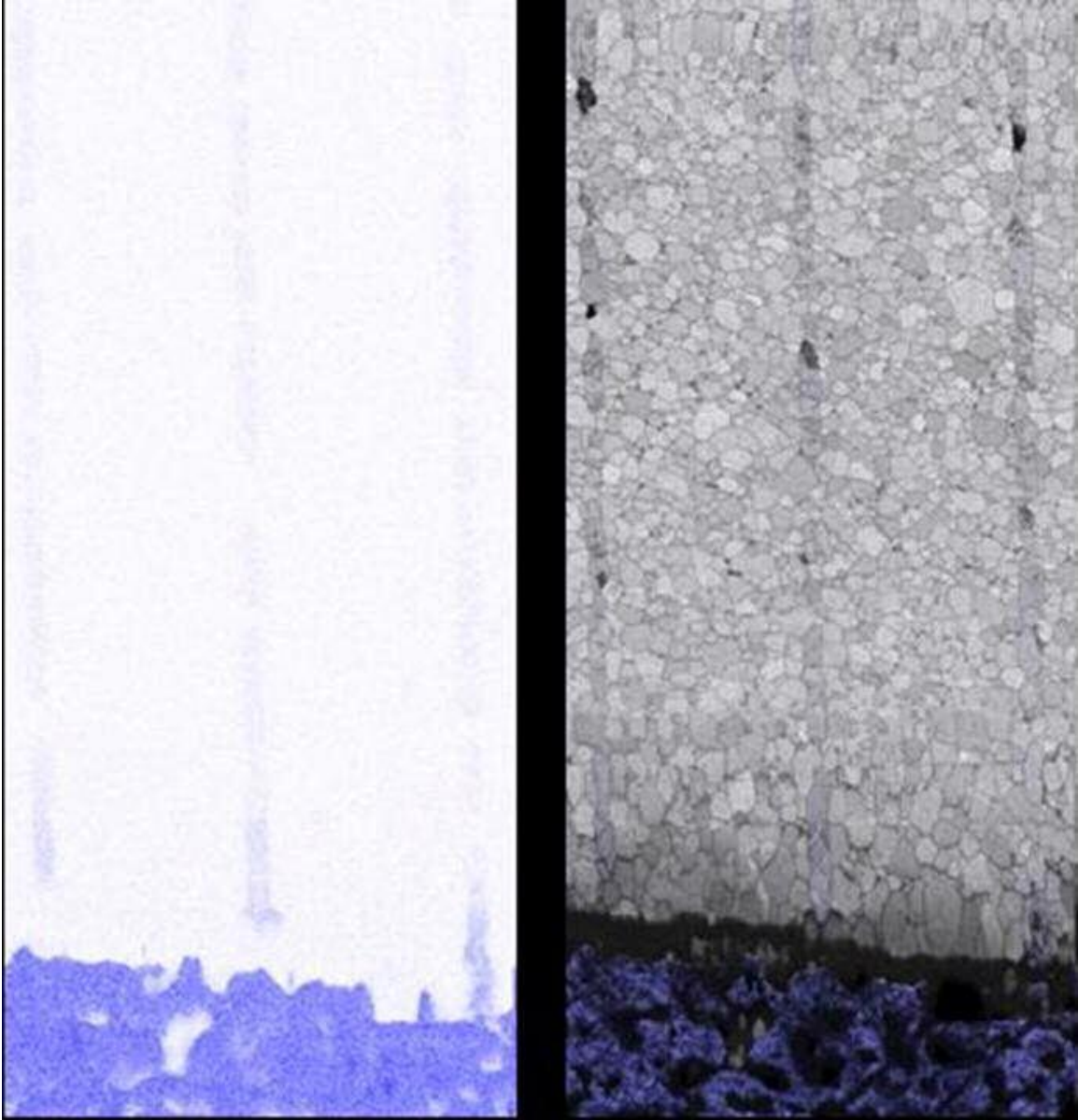
Figure 9: EDS Map of Nickel Electrodes Showing Copper Alloying

The capacitances for all of the capacitors were measured at 1 Volt and 1 kHz using an Agilent 4263B LCR Meter with a 16034G Test Fixture; this is a conventional experimental approach used in the literature [22][20][26]. Measurements were recorded

when the indicated capacitance value stabilized. The capacitance measurements were made at room temperature.

Throughout the experiment, the total time in the environmental chambers and elapsed room temperature measurement time were recorded and logged into a spreadsheet. The computations for elapsed time were also computed by the spreadsheet to guarantee accuracy. In addition, measurement time was kept to approximately an hour during the beginning of testing to minimize introducing sorption[21] or desorption time uncertainty.

Individual capacitors (viz., not mounted to a printed wiring board) were baked in a BMA AH-205 Environmental Conditioning Chamber (Temperature /Humidity) set at 125 ºC. This temperature is at or near the Curie point for Y5V capacitors. The Y5V BME capacitors were baked to remove any moisture for 147 hours. The Y5V PME capacitors were baked for 101 hours. Samples were measured for capacitances and weights immediately after baking in the same manner as previously described.

---

[21] Sorption is the term applied to describe the uptake of atmospheric water when the combined proportions of moisture being taken up by adsorption on the surface or absorption into the bulk [15].

Chapter 5: E<small>XPERIMENTAL</small> R<small>ESULTS</small>

The emphasis in these experiments is identifying and quantifying degradation of capacitance of MLCCs exposed to high humidity and finding the difference in degradation between PME and BME MLCCs. Testing at 121 ℃ and 100% relative humidity is a widely accepted as an accelerated humidity test. It is alternatively called the "autoclave" or "highly accelerated test" (HAST) as specified by IEC 60749-33 [4]. This standard is widely used, because it is an easily created condition adapted to the electronics industry from household cooking. It is a thermodynamic state point for steam as a saturated vapor. The state point occurs at 121 °C and 205 kPa absolute pressure. The temperature is below the Curie point of pure barium titanate and probably below the Curie point of Y5V capacitors. The added pressure of the autoclave should aid in forcing the moisture into pores in the capacitor dielectric and into crevices at the termination to dielectric interfaces, better than the 85/85 test in Table 1. The commercial test chamber used is the ESPEC HAST System TPC-121M. Analysis of variance of the data sets is provided in Appendix B.

5.1: Initial MLCC Humidity Exposure Testing

Room temperature testing at 100% relative humidity was conducted for the array of parts in Table 4. These were selected as a typical selection of common parts. In fact, the EIA 0805 were the parts available out of a long list of parts from a local supplier. The lot date codes were available for the Kemet BME MLCCs and the Murata BME MLCCs. The Kemet BME MLCCs were dated June 1, 2003. The Murata BME MLCCs were dated November 1, 2002.The EIA 1812 parts were provided by a sponsoring corporation. The

purpose of the initial testing was to determine if there was any moisture induced degradation due to humidity exposure. The samples were visually monitored periodically looking for physical cracks. No physical cracking was observed. However, capacitances were measured at the end of the test, and capacitance degradation was noted.

Parts were placed into numbered positions household plastic ice cube trays (one dozen ice cube positions). The plastic ice cube trays were floated on the surface the water in half filled Tupperware® containers, and the Tupperware® containers were sealed by their lids. A small enclosure with open water equilibrates to 100 % relative humidity within a minute or two. Moisture would condense into the ice cube tray, because the room temperature would drop during the winter (when students would secure the lab door into the open position). Therefore, the ice cube trays were dried out approximately once per month.

The results showed that the X7R and Y5V capacitances degraded over time in both the room temperature (RT) and in the autoclave environments. The dielectric spacing between electrodes reflects the voltage rating of the capacitors. Two of the EIA 1812 capacitors have voltage ratings of 630 volts and the approximately 50 micron dielectric spacing reflects this rating implying a dielectric strength. The 25 volt TDK brand 1812 had a voltage rating of 25 volts. The dielectric thickness appeared to be important in determining whether or not the capacitors are susceptible to degradation.

Table 4: Initial MLCC Humidity Testing

Electrode Material	Vendor	Tolerance [%]	Size	Temper-ature Range	Dielectric Spacing [μm]	Nominal Capacitance [nF]	Capacitance after 3500 hours Autoclave [nF]	Capacitance after 4900 hours at RT and 100% RH [nF]
PME	Kemet	±10	0805	X75	17	22	22	21
PME	Kemet	±5	0805	X75	19	10	N/A	9.9
PME	Kemet	±10	0805	X75	30	22	N/A	21
PME	Kemet	+80, -20	0805	Y5V	13	100	N/A	95
BME	Murata	±5	1812	X75	53	100	100	100
BME	TDK	±10	1812	X75	46	100	100	100
BME	TDK	±10	1812	X75	7	10000	860	920
BME	Murata	+80, -20	0805	Y5V	10	1000	710	860
BME	Kemet	+80, -20	0805	Y5V	13	1000	560	610

5.2: Preconditioning Bake: Drying and De-aging

Since, moisture was the variable under study; samples were baked at 125 ℃ over 100 hours to dry out. This changed the capacitances of the samples. This upward change is an apparent de-aging. Table 5 provides a summary of the capacitance changes. The de-aging accounted for a change of approximately 10% across all the samples.

The frequency distribution of the Kemet BME capacitances before and after the baking treatment is shown in Figure 10. The range of capacitances observed is large considering the nominal value of 1000 nF (1 μF) with ranges[22] of 447 nF (a range of 45% of nominal). The initial sample standard deviation is 85 nF. Baking decreases the range to 397 and increases the standard deviation to 103 nF. In addition, the initial (off the shelf) distribution appears truncated. Baking has shifted the distribution to become more normal.

---

[22] Range is the maximum observation minus the minimum observation.

Table 5: Initial Capacitances and Post Moisture Bake-out Capacitances

	Initial Average Capacitance [nF]	Average Capacitance [nF] after Bake at 125 ºC	Percent Change
Kemet BME	881	946	6.9
Murata BME	1154	1246	8.0
Kemet PME	94	106	13
TDK BME	102	107	4.9
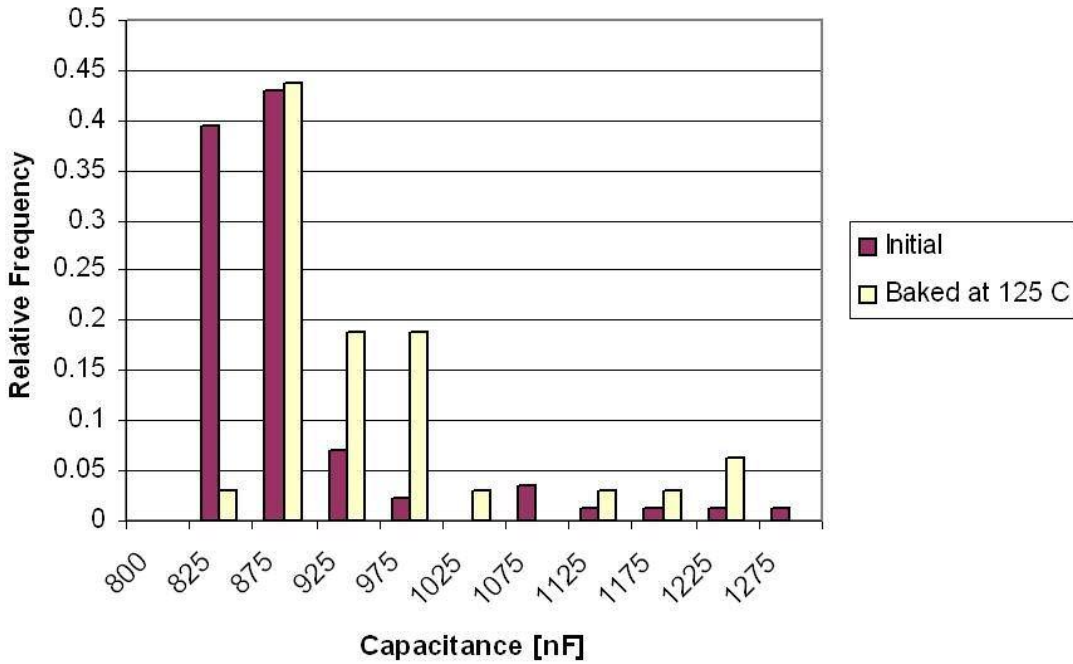
Figure 10: Kemet, 1 μF BME MLCC Capacitance Distributions Showing Shift due to Baking at 125 ºC

The frequency distributions of the Murata BME capacitances before and after the baking treatment are shown in Figure 11, and the plot reveals a much different character than the distribution for Kemet as shown in Figure 10. The range of initial capacitances observed is only 70% of that observed for Kemet (or 25% of nominal). The initial sample standard deviation is only 53 nF. Baking does not change the range, but the standard deviation increases slightly to 61 nF. Both the initial and baked distributions are clearly normal and plot just offset of each other by 92 nF.
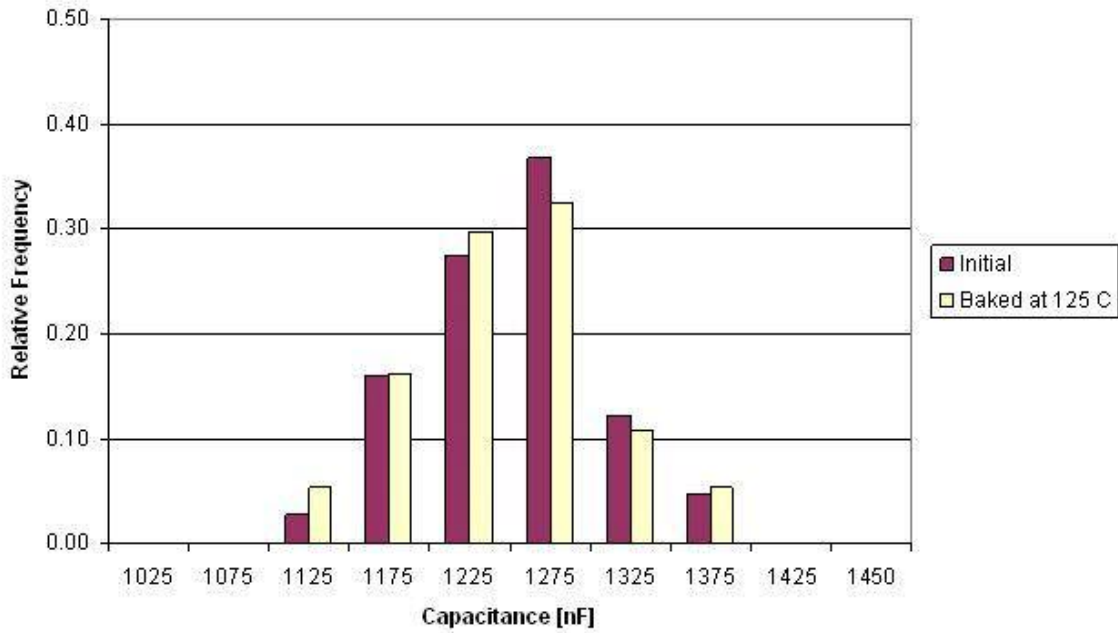
Figure 11: Murata, 1 μF BME Capacitance Distributions Showing Shift due to Baking at 125 ºC

The precious metal capacitors from Kemet in figure 12 show a much different character than the BME capacitors from Kemet. In order to depict the distribution, the ordinate must be a finer scale, 10 times finer. The distributions for precious metal capacitors before and after baking approximate a normal curve.
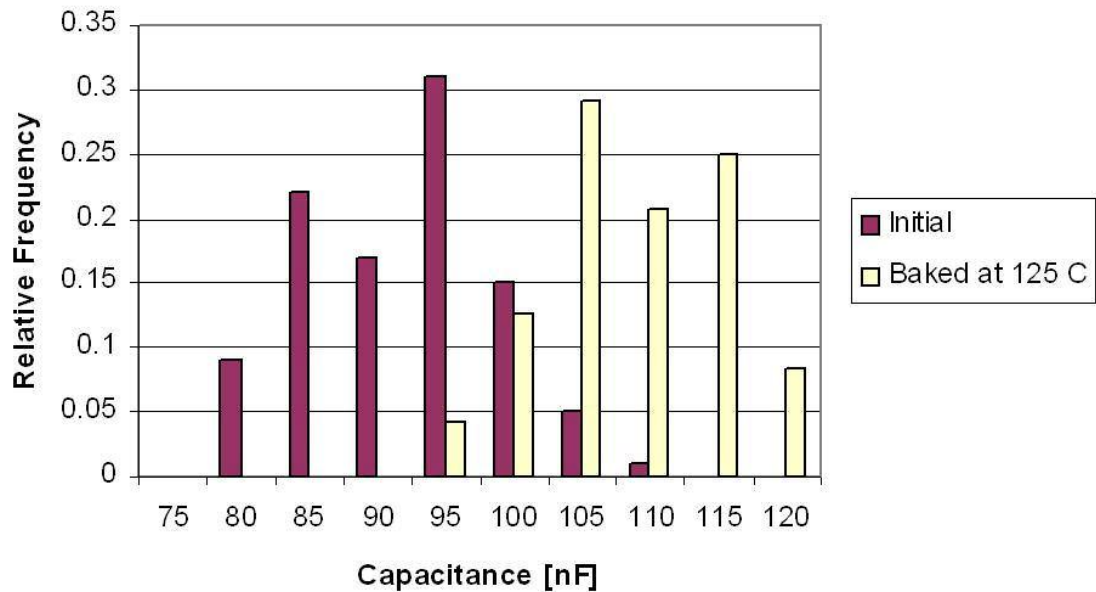
Figure 12: Kemet, 0.1 µF PME Capacitance Distributions Showing Shift due to Baking at 125 ºC

5.3: Accelerated Testing by Autoclave Exposure

Kemet 0805 Y5V BME and PME capacitors, Murata 0805 Y5V BME and TDK 1812 X7R capacitors were subjected to long-term autoclave exposure (over 100 days) with periodic monitoring starting with the de-aged capacitors. The capacitance results are summarized by a series of figures. The figures will begin with analysis of the average for each capacitor and then discuss each capacitor distribution through time. Two types of curve fits will be provided, a traditional aging curve and a best fit exponential curve. Finally, weight change will be discussed.

Figure 13 shows the summary of the three capacitor samples Y5V dielectric as a plot of the normalized sample averages against exposure time. Table 6 provides the

absolute values. Figure 13 shows that the precious metal capacitors only changed 13% in 2600 hours of autoclave, remaining within specification. The two 1 μF BME capacitor averages began at different capacitances, but both averages converge to the same end point, approximately 615 nF at 2600 hours. Since the starting points are different, the plot seems to show divergence when the data is converging. The BME capacitors fell to 64% and 50% of their starting values, both well below specification. Therefore, there is a different result between the BME and precious metal Y5V capacitors when exposed to the autoclave.
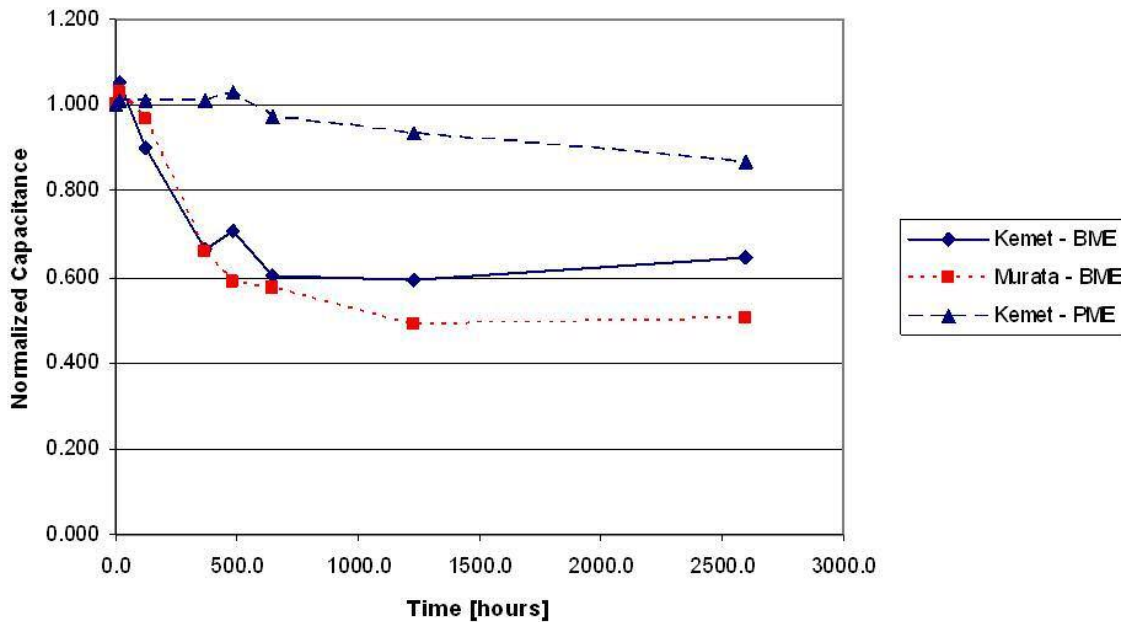
Figure 13: Normalized 0805 Y5V MLCC Capacitance Averages during Autoclave Exposure

Table 6: Autoclave Exposure

Vendor	Electrode Material	Capacitance after 2600 hours in Autoclave [nF]
Kemet	BME	609
Murata	BME	624
Kemet	PME	92
TDK	BME	105

At 2600 hours, monitoring measurements became problematic. The capacitors demonstrate a steady decrease in capacitance. In fact, the decrease in capacitance of follows a third order. This fit was observed ($r^2 \sim 0.99$), but there no effort to formulate a scientific sample size. The capacitance readings steady after a couple of hours. Therefore, due to the difficulty of measurements with the equipment set up, the autoclave test was terminated at 2600 hours.

The distribution for the capacitance readings for the Kemet BME is shown as Figure 14. The figure includes the error bar displaying the range of values observed and the location of the sample average. The shorter bar in the figure legend represents the dashed line (here the dashed line represents 7% aging) in MATLAB® plotting. The number of samples used at each reading is also provided on the plot below the error bars. Two curve fits are shown. One curve fit is the specified worst case aging curve, the 7% aging curve (Table 2) beginning at the average capacitance of the 125 ºC bake. The other is a best fit exponential curve. The coefficient of determination, r^2, is 0.95. The equation is:

$$C = 380 \exp\left(\frac{-t}{225}\right) + 600 \qquad\qquad (3)$$

This type of curve fit also provides a time constant of 225 hours. The testing, therefore, depicts degradation rate for over 10 time constants. This is more than an adequate temporal window to demonstrate the phenomena.
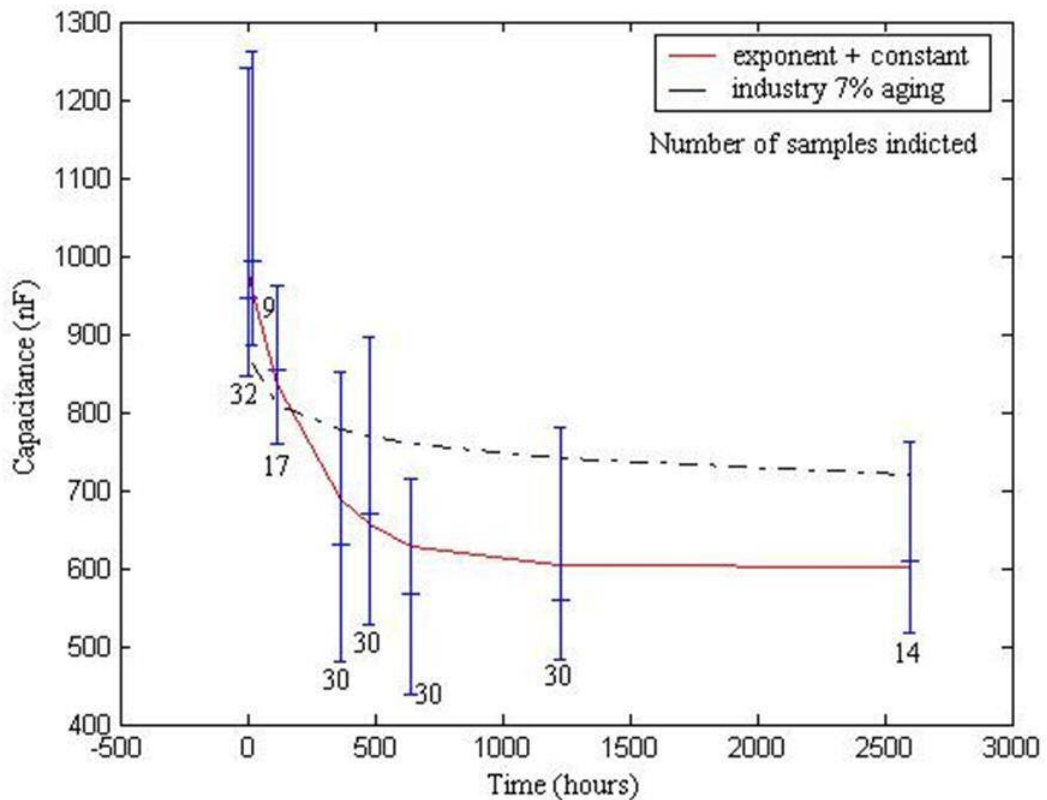
Figure 14: Exponential Curve Provides the Best Fit for Kemet BME MLCCs in Autoclave Environment

Figure 15 provides an alternate curve fit for the capacitance of autoclave aged Kemet BME MLCCs; the curve fit extends the industry standard logarithmic curve fit approach to the autoclave capacitance results. As shown, the best fit using the industry

aging representation shows an increase from the standard 7% aging rate for Y5V (Table 2) to 11%, almost a factor of 2. The coefficient of determination (r^2) for the exponential fit in Figure 14 is 0.95, and the coefficient for the logarithmic fit is only 0.71. The exponential curve fit in figure 15 is worse than the correlation coefficient value of alone implies, because the logarithmic curve fit (figure 15) is trending away from the data at 2600 hours while the exponential curve fit (figure 14) is trending with the data. Therefore, the logarithmic fit will not be suitable for longer exposure times.
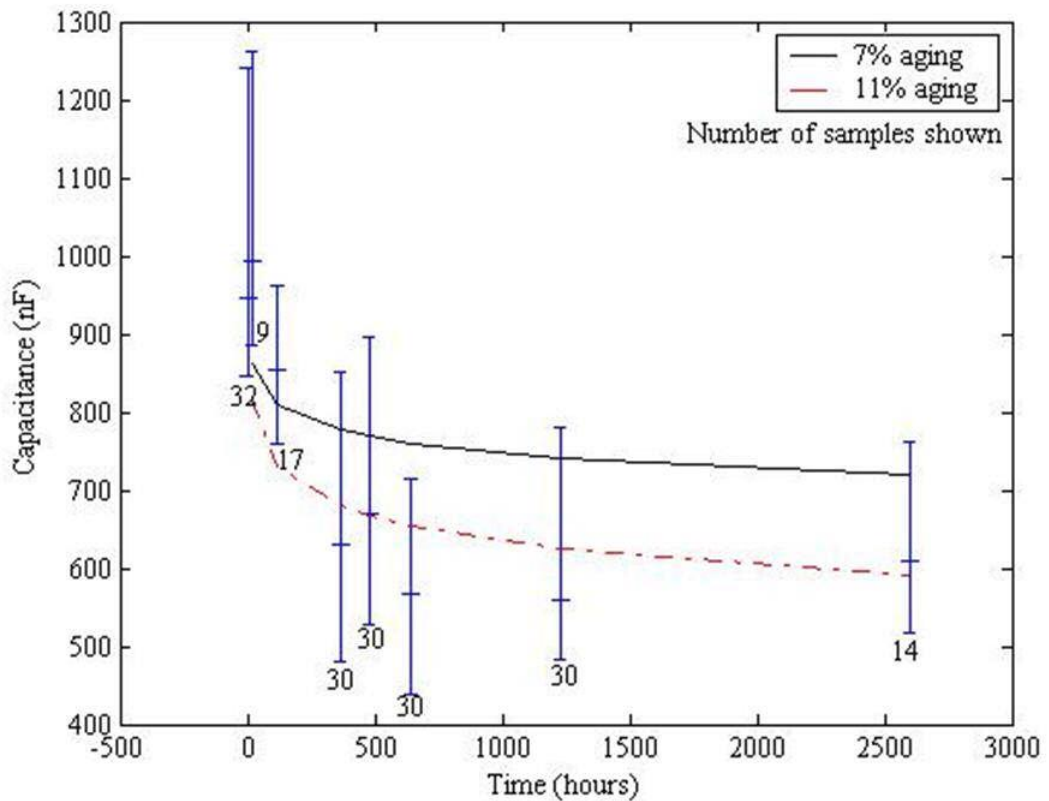
Figure 15: Kemet BME with Logarithmic Curve Fit for Autoclave Data

The distribution for the capacitance readings for Murata BMEs is shown as Figure 16. The figure includes the error bar displaying the range of values observed and the

location of the sample average. The number of samples used at each reading is also provided on the plot below the error bars. Two curve fits are shown. One curve fit is the specified worst case aging curve, the 7% aging curve beginning at the average capacitance of the 125 ºC bake. The other is a best fit exponential curve. The sample coefficient of determination, r^2, is 0.95. The equation is:

$$C = 675\exp\left(\frac{-t}{270}\right) + 610 \tag{4}$$

Comparing the curve fit for Murata BME MLCCs in figure 16 to the curve fit for Kemet BMEs in figure 14, the constant 675 is 1.8 times larger reflecting the higher starting capacitance for the samples of Murata. The final constant (610) differs less than 2% different from Kemet. The time constant is 270, 20% longer. The change in time constant probably reflects a difference in construction.
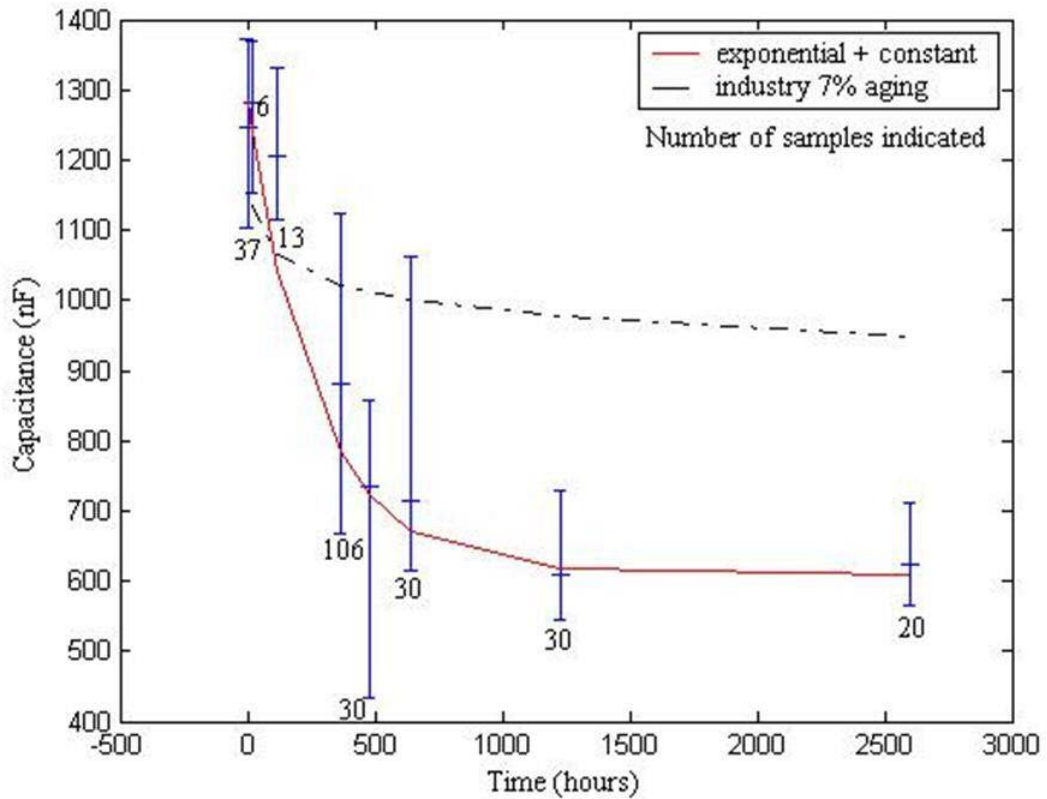
Figure 16: Exponential Curve Provides the Best Fit for Murata BME MLCCs in Autoclave Environment

Just as with the Kemet capacitors in figures 14 and 15, figure 17 provides an alternate logarithmic curve fit to the exponential fit of figure 16; it extends the industry standard logarithmic curve fit approach to the autoclave capacitance results. As shown, the aging rate is increased by exactly a factor of 2 (from the standard 7% to the better fit with 14%). The coefficient of determination for the logarithmic fit in figure 17 is 0.69, and the logarithmic fit is trending away from the data, just as the logarithmic fit trended away with the Kemet data. This indicates the logarithmic fit is not appropriate.
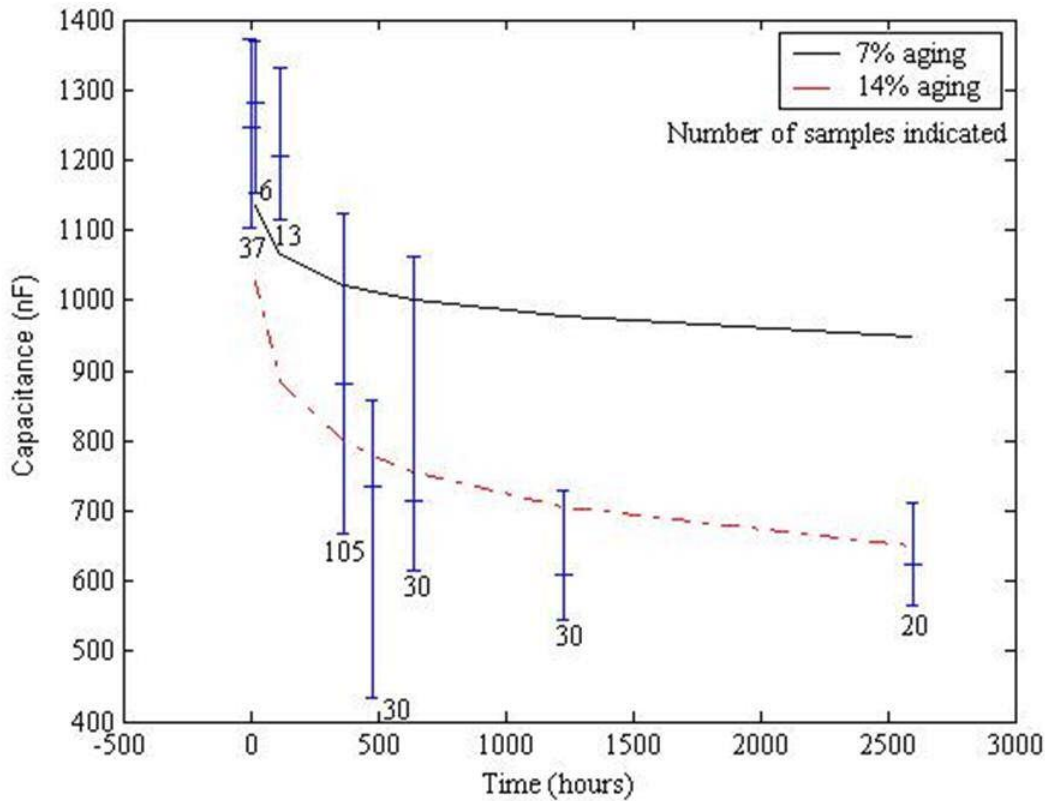
Figure 17: Murata BME MLCC with Logarithmic Curve Fit for Autoclave Data

The precious metal capacitors behaved much differently than the BME capacitors as is shown in figure 18. The scale abscissa is magnified relative to the previous figures in order to not obscure the variation. The final average value was 92 nF. There was one capacitor that fell to 54 nF. This pushes the error bar down, and the high location of the average on the error bar is indicative of this result. The data is similar to the initial observations in Table 4. The data plotted in figure 18 can be interpreted several ways. The data agrees with the logarithmic model of equation (2), because the data remains above 7% aging curve as required. The data could also be explained as an exponential curve with a time constant of approximately 8000 hours. A linear curve fit is plotted in figure 18 and appears as equation (5) and has an $r^2 = 0.89$:

$$C = 108 - 0.0061t \qquad\qquad (5)$$
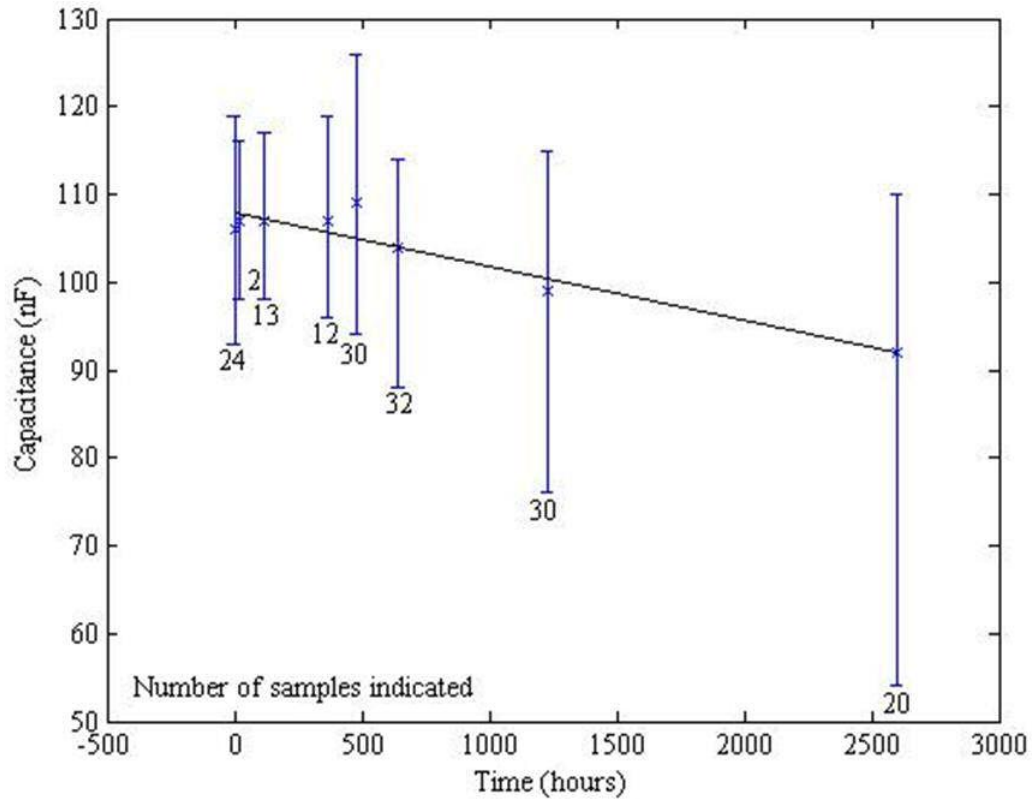
Figure 18: Kemet PME MLCC in Autoclave Environment Reveals Little Degradation Occurred

Figure 19 plots the capacitance for the 100 nF TDK X7R BME in the autoclave. However, this capacitor had a higher voltage rating (630 V vs. 25 V) and a larger dielectric spacing than the 10,000 nF X7R in Table 4 (46 μm vs. 7 μm). The curve fit for the data of figure 19 is:

$$C = 107 - 0.0008\ t \qquad\qquad (6)$$
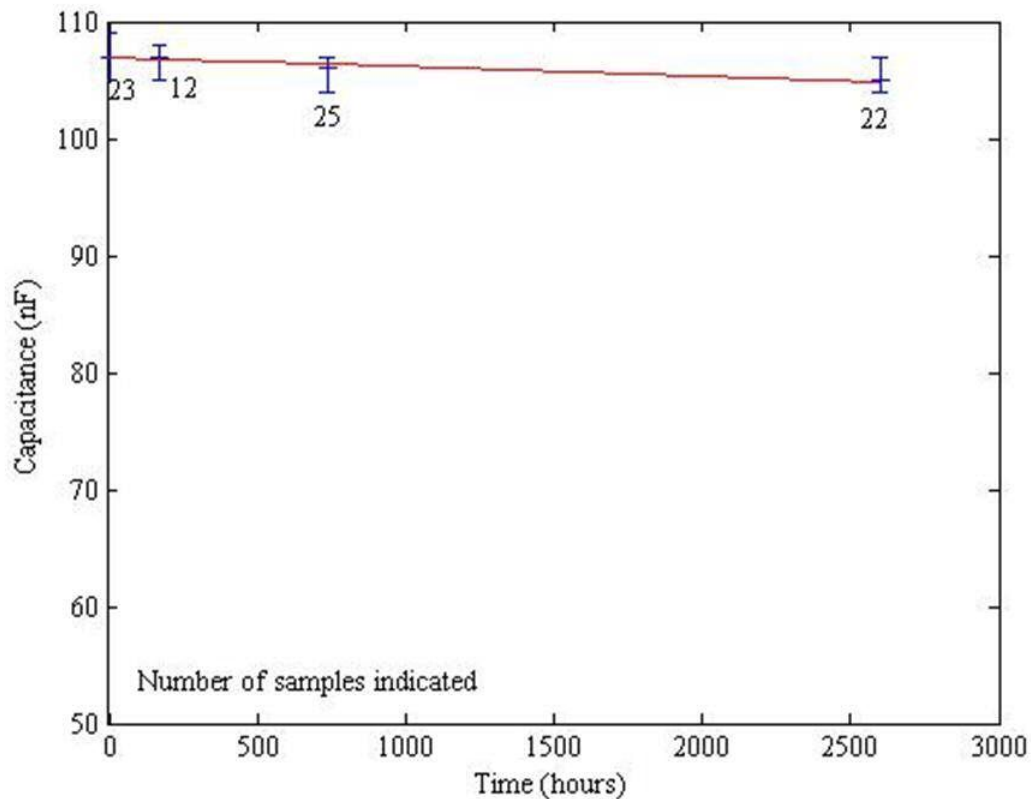
Figure 19: TDK BME Capacitance in Autoclave Exposure Reveals Little Degradation Occurred

5.4: Generalizing Capacitance Degradation from Exposure to Room Temperature with 100% Relative Humidity, to 85 ºC with 85% Relative Humidity and to Autoclave Environments

Section 5.1 described capacitance degradation for two 100% relative humidity environments (room temperature, approximately 23 ºC, and autoclave temperature, approximately 120 ºC). The data of section 5.1 provided only end results. Section 5.3 collected data at intervals for samples exposed to the autoclave environment at intervals, and interval data showed that the degradation was exponential with a time constant. This section adds data for another common testing condition (one of the standard test

conditions in table 1). This condition is 85 ℃ and 85% relative humidity, and it is an intermediate condition between room temperature and autoclave conditions.

Testing of the 0805 BME MLCCs with 85 C/85 % RH conditions was for completed for approximately 1000 hours. First, the samples were de-aged at 135 ℃ for 14 hours. After 1060 hours, the degradation for the 85 ℃/85 RH was compared to the data for autoclave testing. The time at which the autoclave induced capacitance degradation reached the same degradation value as 1000 hours of testing at 85 ℃/85 % RH provides a time ratio called the acceleration factor. Table 7 shows this comparison. Therefore 1000 hours of testing at 85 C and 85% RH can be accelerated to only 125 hours in the autoclave (Table 7). Alternatively, 500 hours at 85 ℃/85 % RH can be accelerated to 60 hours in the autoclave. However, this acceleration is only valid for a small range of time. Therefore, acceleration factors must be applied with duration test and lifetime considered.

The average capacitance degradation data of tables 4 (room temperature testing), 6 (autoclave testing) and 7 (85 ℃ and 85% RH) can be combined to describe capacitance degradation across temperature ranges. As discussed in section 5.3, degradation is governed by a time constant (exponential degradation appears linear for time much smaller than the time constant). The data was fit to approximate[23] exponential fits and plotted. Figure 20 is the resulting plot of capacitance degradation data for Y5V BME MLCCs exposed to (1) 100% relative humidity and (2) room temperature at 121 C and (3) 85 ℃ with 85% RH. The time constants used in these plots were 225 hours for autoclave, 2300 hours for 85 ℃ and 85% RH and 7000 hours for room temperature. Figure 20 includes a straight line for the lower tolerance limit for reference (-20%). In addition, figure 20 includes the standard 7% Y5V aging model from equation (2) with

45

constants from table 2. Clearly the exponential model with it s time constant is superior to the standard logarithmic model. According to this model, degradation due to room temperature and 100% RH exposure will exceed the degradation from the standard logarithmic model at approximately 10,000 hours (1.1 years). In addition, this model predicts that all degradation due to high humidity reaches the same steady state value.

---

[23] Only a couple data points were available for some conditions as shown in the tables.

Table 7: 85/85 vs. Autoclave Acceleration Factor for Small Degradation

	1 μF BME
Final Divided by Initial Capacitance (C/Co) for 85 ºC /85 % RH at 1000 Hours [dimensionless]	0.9
Final Divided by Initial Capacitance (C/Co) for Autoclave at 125 Hours [dimensionless]	0.9
Resulting Acceleration Factor	8.5
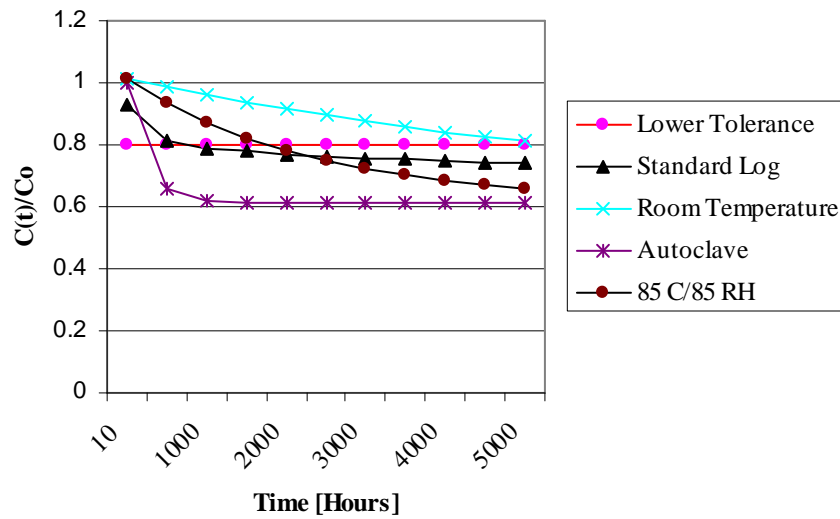
Figure 20: Capacitance Degradation Models, Room Temperature to Autoclave

5.5: Equivalent Series Resistance

Equivalent series resistance (ESR) data was collected for all capacitors. Table 8 summarizes the ESR data. The ESR values began low, and the values increased

dramatically throughout testing. However, the increase was due to oxidation of the solder on the terminations. The oxidation was routinely sanded off to make capacitance measurements, but there was no effort to sand every termination to guarantee the minimum ESR However, the ESR data does show that the terminations did not fail catastrophically as would be indicated by opens.

Table 8: Average Equivalent Series Resistance

	Initial Average ESR [Ω]	Average ESR [Ω] after Bake at 125 ºC	Post Autoclave Average ESR [Ω]
Kemet BME	5.7	6.1	10
Murata BME	5.9	6.0	14
Kemet PME	23	27	57

5.6: Impedance Plot

Figure 21 shows an Argand diagram [10] for the impedance of Kemet BME capacitors based on the measured averages from the autoclave and the vendor specified values. The abscissa (x axis) is the ESR, and the ordinate (y axis) is capacitive reactance. The autoclave data is based on averages for measured values for the frequency range 100 Hz to 100 KHz. The data generates a straight line due to the nature of MLCC impedance. The MLCC acts like a distributed set of resistors, capacitors and inductors. The best model is probably a transmission line [27][28].

The utility of this figure is that it clearly shows the aging effect of the autoclave as a change in slope. The change is controlled an effective capacitance drop after autoclave. The ideas from the field of electrochemistry called impedance spectroscopy apply, but the data from so many plates confound detailed application of the principles.

Nevertheless, the concept of visualizing the MLCC as a network of passive components provides an avenue for intuition.
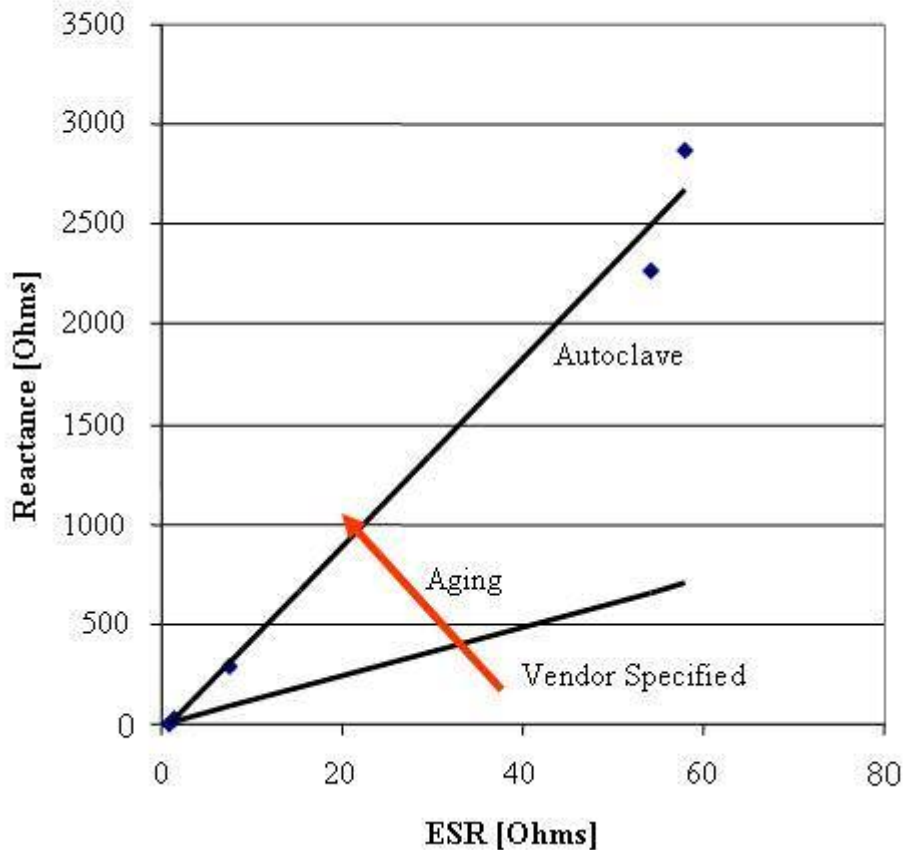
Figure 21: Change in Impedance due to Autoclave for Kemet 0805 Y5V BME

5.7: Reversibility of Capacitance Degradation after Autoclave Exposure

One key question is whether the apparent moisture sorption in the autoclave environment is reversible. If moisture is entering the capacitor material in a sponge-like manner and its presence is the sole reason for changing capacitance, its removal should reverse the effect. However, if the moisture is reacting with the capacitor materials, then it probably cannot be baked out at low temperatures. This can be thought of in terms

used from surface chemistry, physisorption and chemisorption. A definition from the literature is "When a molecule sticks to a surface, it can bind with either a chemical interaction (chemisorption) or a physical interaction (physisorption). Chemisorption involves the formation of a chemical bond between the adsorbate and the surface. Physisorption involves weaker interactions involving the polarization of the adsorbate and the surface rather than electron transfer between them [17]."

Capacitors were removed from the autoclave after 480 hours (approximately two times the time constant) and returned to baking in the chamber at 125 ºC. Figure 22 plots the results for the normalized average capacitance for long term baking (2080 hours) at 125 ºC, normalized to the values at 480 hours in the autoclave. Table 9 provides the corresponding numerical values (Table 5 provides the starting values). The average capacitance PME metal capacitors changed less than 3% from the 480 hours autoclave capacitance value. The average capacitance for the BME capacitors from Kemet increased 7%, but this capacitance value remains 24% below the starting value before autoclave exposure. However, The BME capacitors from Murata degraded an additional 9% in capacitance over the 2080 hours at 125 ˚C. The less than 10% changes, one vendor increased and one decreased, is not important. Comparing the 2600 hour autoclave results for BME capacitors in Table 6 to the autoclave followed by 125 ˚C baking results in Table 9, the time elapsed is almost identical for the 2600 autoclave and the baked samples (480 hours autoclave and 2080 hours at 125 ˚C totals 2560 hours). The resulting capacitances are similar.

Table 9: Average Capacitances before and after Bake-out

Vendor	Electrode Material	Capacitance [nF] after 480 hours in Autoclave	Capacitance [nF] after 480 hours in Autoclave and 2080 hours Baked at 125 °C
Kemet	BME	670	718
Murata	BME	735	667
Kemet	PME	109	106

These results show that the underlying time constant for the PME and BME parts is very important. Once the autoclave induced degradation goes to steady state, it is only partially reversible. The PME parts exposed to the autoclave environment never reached steady state, and their degradation was completely reversible. Neither of the BME parts was reversible back to specification. This hypothesis can be further tested by exposing the samples to a higher temperature, one well above the Curie point. The maximum setting on the baking chamber is 170 °C, so this value was used. The samples were exposed for 91 hours. Table 10 shows that the average of the BME parts changed only 4 nF for Murata's parts and changed only 75 nF for Kemet's parts. Therefore, the figures show that aging in the autoclave is not reversible (using the standard de-aging practice of heating above the Curie point, even for long durations or at 170 ºC) as would be expected for aging.

Table 10: Average Capacitances for 170 °C Bake-out

Vendor	Electrode Material	Capacitance [nF] after Continued Baking at 170 °C
Kemet	BME	793
Murata	BME	663
Kemet	PME	117
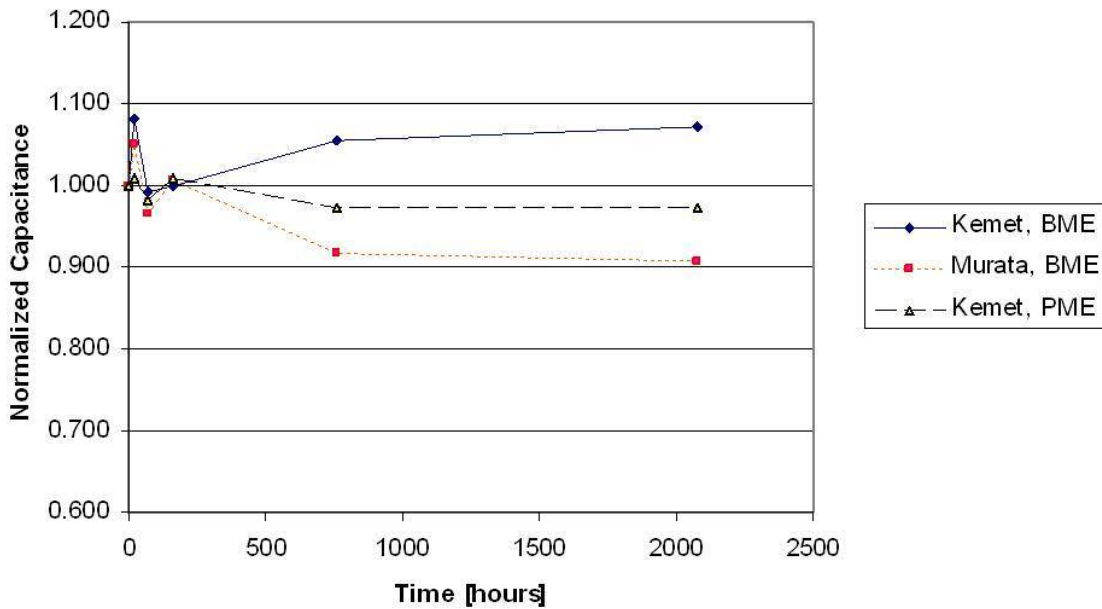
Figure 22: Baking 0805 Y5V MLCCs at 125 °C after 480 Hours of Autoclave

5.8: X-Ray Photoelectron Spectroscopy of BME MLCC for Nickel Oxide

One hypothesis for MLCC capacitance degradation due to moisture was oxidation of the nickel electrodes. Spectroscopy was conducted in order to further seek the root cause of capacitance degradation, because the change in capacitance observed in the phenomenological plots of capacitance against time were most likely caused by a chemical change. One way to test for oxidation is by using x-ray phototoelectron

spectroscopy, or XPS. The University of Maryland has an XPS in the Chemistry Department. It is a Kratos AXIS 165 X-ray Photoelectron Spectrometer. The XPS is equipped with an argon ion etch gun.

From the University of Maryland web site provide a brief description of the operating principles of XPS: "X-ray phototoelectron spectroscopy is a widely used method of determining the chemical composition of a surface. The analysis is done by irradiating a sample with soft x-rays to ionize atoms and releasing core-level photoelectrons. The kinetic energy of the escaping photoelectrons limits the depth from which it can emerge, giving XPS its high surface sensitivity and sampling depth of a few nanometers. Photoelectrons are collected and analyzed by the instrument to produce a spectrum of emission intensity versus electron binding energy. Since each element has a unique set of binding energies, XPS can be used to identify the elements on the surface. Also, peak areas at nominal binding energies can be used to quantify concentration of the elements. Small shifts in these binding energies (chemical shifts) provide powerful information about sample chemical states and short-range chemistry" [43]. The XPS measurements were made at $8x10^{-8}$ Torr (0.1 µPa) with non-monochromatic Mg Kα radiation. The x-ray power was set at 144 W. The sample was mounted on conductive carbon tape. All measurements were taken in hybrid mode using both electrostatic and magnetic lenses with a step size of 0.1 eV.

A Kemet BME capacitor was spit in half using the MLCC cleaving tool (figure 1) revealing the nickel electrode plates end-on. Nickel is always found oxidized in the atmosphere, so etching would be required. There were five repeated 15 minute etches followed by data recording cycles. The depth profiling was done at a pressure of $5.6x10^{-7}$

Torr (0.75 μPa) and the argon ion etch gun set at 4 kV and 20 mA. The XPS does not provide quantitative information on the depth of etching. Reviewing the NIST XPS data base for nickel compounds, the spectral data is fit to molecular bonds. The data that best first the profiles is shown in the following table. Figure 23 shows the measured intensity in counts per second.

Table 11: XPS Results for Cleaved Post Autoclave Kemet BME

XPS Spectral Line Description	Bonding Energy [eV]
Ni 2p 3/2	852.3
NiO 2p 1/2	871.8
NiO 2p 3/2	854.3
Ni 2p 1/2	879.8
Satellite Peak	874.4
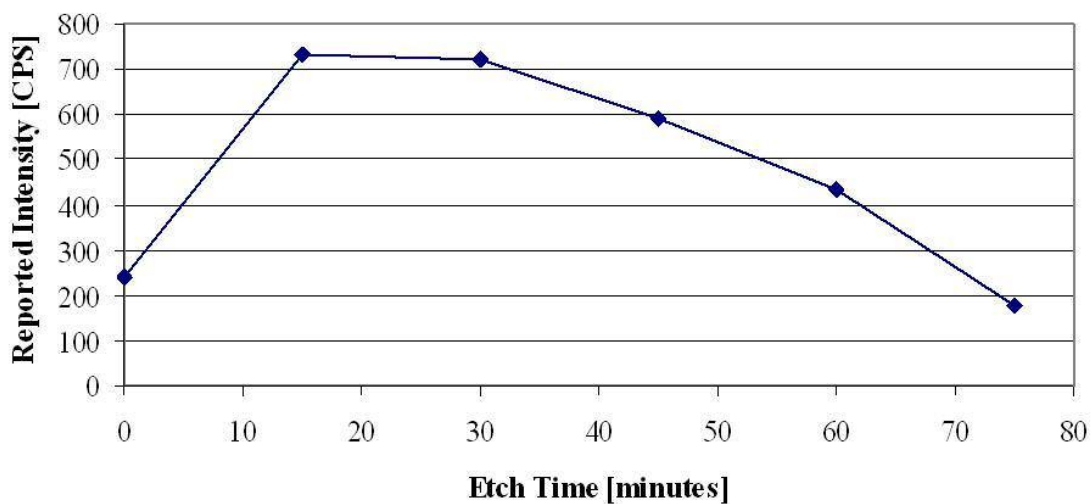
Figure 23: XPS Data Shows Reducing Nickel Oxide with Etching into Capacitor Body

Figure 23 shows that the CPS of the dominant binding energy for nickel oxide. The first data point on the surface include all the chemisorbed and physisorbed species remaining after an overnight vacuum soak, and it can be ignored. The data for the remaining etches shows that the nickel oxide quickly is removed as the ion etch progresses. Therefore, the ion etch showed that the oxide layer is not present within the bulk.

Table 12: NiO Atomic Percent with Etch Time

Etch Time [Minutes]	Atomic Percent NiO
0	45
15	18
30	15
45	11
60	8
75	7

5.9: Moisture Ingress Investigations into MLCCs by Dye Penetrant Testing and by Weigh Gain Analysis

Two sets of experimental efforts investigated moisture ingress. First, dye penetrant testing was conducted using two different dyes. When these experimental results did not reveal moisture ingress, another dye penetrant test method was investigated. The dye penetrant methods used or considered for use during this thesis effort will be outlined in the following text in the hope of aiding future researchers. In parallel to the dye penetrant testing, weight gain measurements were undertaken. These weight gain methods and the results of the weight gain efforts will follow the discussion of dye penetrants. The dye penetrant efforts and weight gain analysis are complimentary to a scanning electron microscopy method called electron backscatter diffraction. All these methods pointed in one direction. Moisture was not flowing into the capacitor bodies; moisture was not flowing as a fluid.

Magnaflux® (a Division of Illinois Tool Works, Inc.) Zyglo® ZL-4C is a widely used fluorescent water soluble penetrant (based on discussions with Dr. Ganesan and Janet Quinn at the National Institute of Standards and Technology, NIST). According to the Material Safety Data Sheet (MSDS), Zyglo® has the beneficial properties of being biodegradable and forming a non-hazardous waste (reference to the most recent MSDS

through Magnaflux® and reference to ultraviolet (UV) safety procedures is recommended). Telephone conversations with the company's staff confirmed that the penetrant was appropriate for this water penetration study. Zyglo® ZL-4C is supplied in 5 gallon containers. Zyglo® ZL-4C is diluted in water in a ratio from 1:1 or 1:2 before use. It was procured through V.O. Baker Distributing Company in Mentor, Ohio. Zyglo® is manufactured to be visible as bright green-yellow in color when illuminated by ultraviolet light centered at 365 nm. This wavelength falls within the spectrum called UVA (315nm to 400 nm); the conventional name is black light (approximately 350 to 400 nm). A low cost commercial black light was procured, and drops of Zyglo® did produce a brilliant yellow-green when illuminated by the black light.

MLCC samples were soaked in the diluted penetrant and cleaved (figure 1) for microscopic inspection for moisture ingress into the MLCC body. The black light did not provide sufficient illumination of the sample, even with an opaque shield over the microscope and operator. Purchase of alternative illumination methods were investigated, but, after talking to several vendors, the acquisition price of appropriate commercial microscope equipment was judged to be too expensive (in excess of $10,000). Alternative university resources were investigated. A meeting with the Tim Maugel, Director of the tour of the University of Maryland Biology Department's Laboratory for Biological Utrastructure, uncovered that his equipment had a too narrow depth of focus for inspection of MLCCs.

Therefore, two alternative penetrants were investigated. Use of a common biological stain known as Methylene Blue (MB)[24] was suggested by Norm Helmold of CALCE. A small amount of MB was graciously provided by the University of Maryland Animal and Avian Sciences (ANSC) Department. A stock solution of was made with the ratios of 1.4 grams of MB in 100 ml of 95% ethyl alcohol as recommended by Ms. Nichola Thompson of ANSC. A working solution was produced by adding 10 ml of stock solution to 90 ml of de-ionized water. Capacitors were soaked in this solution for over a month. Inspection under the microscope showed no observable penetration, but the blue color was not too far from the gray to brown shades of MLCC dielectric. Work on yet a third method of die penetrant testing was initiated based on the use of the standard for die pentrant testing using a facility at Freescale Semiconductor, Inc. in Austin, Texas per ASTM F 97-72 [81]. However, the results of the previous penetrant testing combined with the evidence from the EBSD (section 4.3) and combined with the results of the weight analysis described below all pointed to the fact that moisture was not flowing into the MLCC body. Therefore, efforts to continue research using penetrant testing were discontinued before traveling to Austin.

When capacitors were taken from the as-supplied condition and dried in a temperature chamber set at 125 ºC for 147 hours as described in section 5.2, they were weighed using a Mettler AE 100 balance. The samples were then were weighed again after baking. Table 13 shows the change in weight.

---

[24] Methylene Blue is the generic name for the biological staining agent produced by Sigma Chemical Company (St. Louis, Missouri) stock number M-1459, CAS No. 61-37-4.

Table 13: Moisture Weight Gain

Capacitor Type and Brand	Number of Samples	Initial Average Weight [g]	After 147 hours at 125 °C Average Weight [g]	Percent Weight Change
0805 Kemet BME	86	16.726	16.678	0.3
0805 Kemet PME	100	13.765	13.738	0.2
0805 Murata BME	106	10.849	10.814	0.3

A simple validation experiment was attempted again using a more precise balance, a Mettler Toledo AX105. Measuring the mass of two Murata BME capacitors baked at 170 C in a series of 4 measurements over a 72 hour period resulted in similar results. Both samples showed weight changes in the 4th decimal place that were increasing and decreasing.

Thermogravimetric Analysis using the Shimadzu TGA-50 was completed on the Murata BME samples with most of the solder removed by sanding. The samples were taken off the reel and heated to 600 °C. Both air purges and argon purges were used, because the air data may have included oxidation reactions of the solder with air. The results showed that there was no measurable weight gain from the reel.

Table 14: TGA Beginning and Ending Mass

	Beginning Mass [g]	Final Mass [g]
Air Purge	10.47	10.45
Argon Purge	10.28	10.28

Leygraff and Grandel [54] provide a summary of the numbers of monolayers of atmospheric moisture on various surfaces. For example, they claims that the surface of lead is described as being mostly lead oxide with at least 5 monolayers of lead at 70% relative humidity and of at least 10 monolayers of water at 100% relative humidity. Using this concept, the weight of water on a 0805 capacitor due to surface moisture can be estimated. This estimate can be compared to the sensitivity of analytical balances available.

The Murata BME capacitor dimensions are 2.0 x 1.25 x 0.85 mm. Based on an estimate of the mass of water on the surface from first principles, the weight changes due to moisture may be difficult to detect. Calculations assuming water (18 g/mole) bound to ceramic set an upper bound, because water must disassociate into hydrogen and oxygen in order to form bonds with either ceramics or metals. The Van der Waals diameter of water is 0.32 nm. The densest packing yields: 2 mm/0.32 nm = 6.25e6 atoms along length, 1.25/0.32 = 3.91e6 along width, 0.88/0.32 = 2.66e6 along thickness, totaling 1.03e14 atoms for a surface monolayer. Estimating the mass of a monolayer of water: (1.03e14/6.022e23 moles)(18.0152 g/mole) = 3.1 ng for oxygen This molecules/area value is reasonable, i.e. 15 times higher than the order of magnitude baseline estimate for gas on an evaporated film adsorbent in the literature [74]. Even though the surface may have several monolayers due to physisorption, the surface mass is too small to be measured with typical scales.

The experiments show that the amount of moisture change is insignificant in terms of bulk water gain or loss. However, the evidence in following paragraphs will show that there may be some atomic changes beyond the ability of measurement.

Chapter 6:   EXPLANATION OF CAPACITANCE DEGRADATION IN BME MLCCS

As described in Chapter 5, the capacitance degradation of BME MLCCs exposed to 100 percent humidity did not follow the logarithmic aging rule of equation (2) for barium titanate MLCCs. The aging rule describes a phenomenon due to coupling of ferroelectric and mechanical responses to volumetric changes due to phase changes during cooling [18] [39]. Instead, a new hypothesis for the degradation mechanism is needed. Direct moisture ingress by flow through porous media was rejected due to the density of the sintered body, a manufacturing goal for MLCCs. The hypothesis that the nickel capacitor electrodes were corroding due to ionic oxygen has been investigated by successive ion etch analysis using the XPS, and the hypothesis was rejected. However, there is a wealth of literature for past investigations on an alternative mechanism; oxygen vacancy ordering along domain walls will be described below. This will be shown to be the best explanation of the mechanism for BME MLCC degradation exposed to high humidity. This explanation is based on a proof by elimination of hypotheses.

One of the interesting features of this body of work is the synergy of all the approaches to measuring the electro-mechanically coupled properties of the ferroelectric oxides. In addition, the researchers come to this problem from the perspectives of chemistry, geology and practical electronics.

Ceramics contain defects, and some of these defects continuously interact with the environment. The reduction of an oxide in a ceramic oxide such as barium titanate is expressed as

61

$$O_O = \frac{1}{2}O_2(g) + V_O^{\bullet\bullet} + 2e' \tag{7}$$

where the "O_O" refers to oxygen at an oxygen atom site, "V_O" refers to an oxygen vacancy at the site of an oxygen atom. The two dots imply a double positive charge. In this equation, oxygen is released to the atmosphere as a gas and two electrons are released into the solid. Not all ceramic oxides will readily reduce in this manner. For example, alumina has cations of fixed valence for which the oxide bond involve a large amount of energy. However, transition metals such as titanium are multivalent and will allow oxygen deficiencies of over 1% before changing phase or disassociating [77]. As discussed previously (in the Introduction and in Appendix D), the firing operation of the BME MLCCs creates more initial oxygen vacancies than air firing of PME MLCCs.

The consequences of the reactivity of barium titanate in terms of capacitance have been reported in the literature for 50 years. Anderson et al. at Bell Laboratories in 1955 briefly discussed their simple phenomenological experiment in which they monitored the 60 Hz hysteresis loop for a 0.1 mm single crystal of barium titanate. They powered their capacitor for periods on the order of an hour in dried air, vacuum (10^{-6} mm Hg), helium, hydrogen (H_2), oxygen (O_2) and water vapor environments on the response of a barium titanate capacitor. They claimed that water vapor and H_2 were both reducing agents [56].

Nomura et al. [1996] state that there are residual electric fields in the dielectric caused by migration of oxygen vacancies. They, and others [52], discussed the need for donor dopants to offset the effects of oxygen vacancies [67].

The nature of the interaction of oxygen vacancies with the crystal is complex, because there is a substructure within each crystalline grain. Ferroelectric crystals order into ferroelectric domains. The subdomains occur in order to minimize the energy associated with the surface charges arising after spontaneous polarization of the unit cells. The domains are made up of many parallel oppositely polarized regions, a process called twinning [39]. The standard aging phenomena is the interaction of the domains with the mechanical stress field [18] [68]. The domains have an associated size which is still being investigated as potentially setting the limits of possible miniaturization [71]. The domains are on the order of 5 to 20 µm [39]. Domain walls in barium titanate are thin, on the order of 15 to 20 Å [69]. To summarize, "the mobility and motion of these domain walls plays a decisive role" [70] .

Warren et al. studied the effects of reducing ambient conditions on remnant polarization in single crystals of barium titanate, similar to, but more extensive than, the work of Anderson et al. Warren discussed the role of oxygen vacancies in reducing the net capacitance by electron paramagnetic resonance spectroscopy (EPR). Warren et al. used vacuum (0.65 Pa after an argon gas purge to remove oxygen, reporting a partial pressure of oxygen of 10^{-6} atmospheres) at 600 ºC as their "slightly reducing" environment. They used a forming gas (5% H_2 and 95% N_2, reporting a partial pressure of oxygen of 10^{-13} atmospheres) over temperatures ranging from 500 ºC to 650 ºC as their "strongly reducing atmosphere". They removed and reinstalled charges and monitored the changes to the iron ion (iron is a contaminant in the titanium position) by EPR. They also measured polarization before and after exposing the crystal to the reducing

environments. Their results showed that oxygen vacancies are trapped at domain walls resulting in reduced capacitance in crystalline barium titanate [72].

The work by Scott and Dauber [73] discussed how to gather more direct evidence of oxygen vacancy ordering as a fatigue mechanism in perovskites. They provided a helpful figure, a two dimensional projection for the growth of oxygen order vacancies along the (101) plane from an isolated defect to a dimmer and onto a trimer. They proposed nuclear magnetic resonance (MNR) and Mossbauer Effect (sensitive gamma ray based spectroscopy for certain atoms) studies to demonstrate this mechanism.

McCammon et al. [48], an international collaboration of geologists, did perform an elaborate battery of experiments along the lines proposed by Scott and Dawber. Their interest was in polycrystalline perovskites $CaTiO_3$-$CaFeO_{2.5}$. Their goal was to extrapolate the results to other more geologically interesting perovskites. They performed x-ray diffraction, Mossbauer spectroscopy, infrared spectroscopy, transmission electron microscopy (TEM), electron loss spectroscopy (EEELS), neutron diffraction and electrical conductivity methods. They provide a 3 dimensional figure explaining their findings. Their work is consistent with the figure and the approach suggested by Scott and Dauber. They note that oxygen vacancy ordering resulted in a 25% reduction in the bulk modulus. They also echo others that there should be fatigue (viz., aging) of the ferroelectric properties. The oxygen vacancy ordering process they propose is (1) disordered vacancies, (2) clustering into chains of increasing length, (3) formation of infinite chains along the <101> direction, (4) nucleation of planes into domains, (5) coarsening of domains into twins, (6) creation of a fully ordered structure of planes {0k0} made up of chains along <101> directions.

Cheng et al. [70] continued similar work using vacuum annealing barium titanate by mechanical spectroscopy. Their measurements of elastic modulus and mechanical loss factor were taken over the temperature range of 60 ºC to 150 ºC at 0.3 Hz. Their two redox (reduction – oxidation) environments were vacuum (2 Pa) at 700 ºC (with one confirmation test at 900 ºC) and air at 650 ºC. They argue that they have direct evidence of oxygen vacancies pinning the motion of domain walls.

These references provide a body of knowledge gradually expanding the understanding of ferroelectric fatigue of perovskites (barium titanate) over 5 decades. Researchers have used many approaches, but the pivotal role of oxygen and oxygen vacancies has remained a common thread. In this thesis, the important role of the reducing nature of moisture has resurfaced from Anderson's observations in 1955 to the attention of researchers of BME MLCCs. The theory proposed in this thesis is that the BME MLCCs have a large number of oxygen vacancies remaining from firing. When the MLCC is exposed to high humidity, additional oxygen vacancies are created on the surface. Therefore, a concentration gradient is created from the surface to the center of the capacitor body, and motion of the oxygen vacancies results. Oxygen vacancies arrange into an order along ferroelectric domain walls, because this is a lower energy state. The result is a lowered net capacitance.

Chapter 7: SUMMARY

The capacitor industry is a process industry driven by the economies of large scale production. The transition from precious metal electrodes to base metal electrodes was a necessity in the normal cost reducing evolution along the learning curve in high volume markets. Multilayer capacitor demand will continue to grow, because the MLCC is a required component for signal conditioning in high speed digital electronics.

This thesis presents experimental data for moisture exposure in an accelerated test, the autoclave test. The results show that capacitors degrade in the autoclave environment. The extent of degradation of BMEs was more than was found for precious metal capacitors. Therefore, there is some degree of reliability risk, although the risk may be small, in using the BME parts in humid environments.

The capacitor industry's standard 85 ˚C/85% RH testing for 500 (to 1000 hours, varying with vendor) allows a $\pm$30% change as their success criteria. The BME results in the autoclave exceed this test failure criterion in less than 500 hours. Projecting out, the PME would require approximately 8000 hours reaching 30% degradation. Therefore, results show that there is a significant difference between the PME and BME degradation due autoclave exposure. This difference is underscored by a difference in apparent time constants. The industry standard logarithmic rule does not predict the degradation process very well.

Given that there is a clear difference in degradation, something related to physical construction is significantly different between the BME and PME capacitors. Sample

cross sections were analyzed by optical microscopy and by scanning electron microscopy after by being cleaved into two halves or being cross sectioned and lapped. These analyses provided dielectric thicknesses. FIB and EBSD were used for better identification of the body and surface topologies, respectively. These analyses showed that the capacitors were not sufficiently porous to promote moisture migration. This conclusion was supported by weight gain and loss measurements, however the weight change was almost certainly below perception levels. The likely cause was hypothesized to be due to oxygen vacancy motion within the capacitor body. XPS analysis showed that the nickel electrodes were not oxidizing within the body. Therefore, the best hypothesis, based on the weight of evidence through the literature, is the motion of oxygen vacancies.

Chapter 8: CONTRIBUTIONS

This work provides the first comprehensive study of humidity degradation of base metal electrode multilayer capacitors in high humidity. Until now, companies have used standardized qualification and life testing based on past experience with air fired precious metal electrode capacitors.

The contributions of this work can be summarized as the following:

- Demonstrated a new time dependent degradation phenomena in barium titanate based ceramic multilayer capacitors with base metal electrodes and showed that precious metal electrode capacitors are not susceptible to this type of degradation

  o Provided phenomenological data for the degradation process in room temperature, 85 °C with 85% RH and autoclave environments and predicted that they all eventually reach the same equilibrium.

  o Showed the degradation is not reversible (known "aging" is reversible)

- Demonstrated that industry standard 500 hour humidity testing is not long enough to observe this new degradation mechanism

  o Provided acceleration factors for standard test conditions

- Invented a nondestructive sorting method to separate base metal electrode capacitors from precious metal electrode capacitors (patent applied for)

- Defined and performed testing for several alternative hypotheses that might describe base metal electrode degradation

- o Moisture ingress can degrade capacitance. Using analysis by focused ion beam and scanning electron microscope and texture analysis by electron backscatter diffraction, determined that the capacitor structure did not have interconnected voids required for moisture transport as a fluid flow. Additional weight change measurements further confirmed that there was no moisture.

- o Degraded capacitance due to swelling electrodes from oxidation of nickel was also eliminated. Analysis by x-ray photoelectron spectroscopy with multiple ion etches showed that the nickel electrodes were not oxidized in the body of the capacitor after autoclave. Therefore, oxidation of the electrodes was not the root cause.

- Showed from the literature that capacitance degradation of barium titanate capacitors due to ambient conditions has been known and demonstrated for almost 5 decades, but it had not been attributed to degradation of base metal electrode capacitors. Theorized that the chemistry causing the degradation is oxygen vacancy ordering at ferroelectric domain walls and that this effect results in reduced capacitance.

- Derived the Ellingham Diagram to show the thermodynamic origin of the reduction of barium titanate during sintering that creates oxygen vacancies.

Chapter 9: FUTURE WORK

This thesis has generated opportunities for future work; a few opportunities for fruitful work will be outlined in the following paragraphs.

- The degree of MLCC degradation is related to the dielectric thickness. This effect can be inferred from table 4 (and from the other autoclave exposure tables). Investigation paths include researching mechanical stress differences and measuring differences in the ferroelectric domain structures by appropriate methods of spectroscopy.

- A larger set of MLCCs could be tested in high humidity environments to create a complete nomograph [82] for humidity degradation that could include description of temperature-humidity duration rates across MLCC sizes.

- The work could be expanded to smaller capacitor sizes to test if the smaller sizes are more vulnerable to humidity induced degradation as was hypothesized.

- A study could identify what temperature might de-age BME MLCCs after humidity degradation. The data of table 18 provides a starting point for heating somewhere approaching 1000 ºC.

- Formulate and fire Y5V dielectric using the BME process as described in the patents to create simple capacitors. These capacitors can be exposed to the oxygenating and reducing atmospheres and also used for mechanical resonance testing as discussed in the references.

Appendix A: Crystallography for EBSD

The figures in this report use standard descriptions and representations from the field of crystallography. Since this terminology is not standard to most experts in the electronics field, this brief appendix will provide an overview of the main concepts.

Crystalline solids are defined as an ordered arrangement of repeated molecular structures called unit cells. Large numbers of unit cells form a crystal. Most ceramic materials, such as barium titanate capacitor dielectric, are formed of many small crystallites called grains. The ceramic materials are therefore referred to as being polycrystalline. Mechanical and electrical properties depend on how these grains are arranged in the polycrystalline material. Electron Backscatter diffraction (EBSD) provides what is called crystallographic texture [31], the sample's preferred grain orientation and grain size.

The unit cells have shapes such as tetragonal (rectangular), the case for room temperature barium titanate. The unit cell has sides with dimensions in the Cartesian coordinate system (vectors x, y and z) named a, b and c. In the case of tetragonal barium titanate a=b, so there are only a and c directions. The c direction is taken as the longer direction. The direction along the c axis is referred to using the notation [001]. Similarly, the a direction is [100]. Other directions are made up in a similar fashion. Sides of the unit cell are all similar, and family's crystallographically similar directions are designated, for example <100> refers to all the Cartesian axes [33].

Texture is described by what are called a pole diagram. The normals to crystal planes such as unit cell faces are called poles. The pole diagram is constructed as follows. First imagine a unit cell (or a single crystalline grain) placed at the center of a reference sphere. The axes of the unit sphere are the most convenient coordinates from the sample x, y and z. For example, these might be the length, width and face of a cross sectioned capacitor body. Second imagine a normal being drawn from any face to intersect with the sphere's surface. Third, imagine a line drawn from that intersection point on the sphere to the bottom of the sphere along its axis, i.e., south pole of the sphere. Fourth, the intersection point on the equatorial plane of the line along from the sphere surface to its "south pole" is the representation of the normal (or pole) on the unit cell. The equatorial plane in the plan view (as in the drafting convention) with all poles drawn as points is called pole diagram. Note that normals from the unit cell in the lower hemisphere are projected to the "north pole." Often the pole figure will represent only a subset of all poles. For example, the poles may be only the poles for the family <100>. In all cases the pole diagram relates the unit cell poles in the grains to the sample coordinate system. [34].

The inverse pole diagrams describe the sample with respect to the crystal coordinate system rather than the sample coordinate system. The inverse pole diagram is based on mapping all directions onto a spherical triangle by crystal transformations. The spherical triangle makes up only one twenty-fourth of the reference sphere. The legend uses a representation of times random explained as follows. "When a pole figure or inverse pole figure is created based on a calculated orientation distribution function (ODF), the red region in each plot represents a peak of high intensity. It correlates to a

cluster in a discrete plot. The height of the peak provides a quantitative measure of the amount of clustering. The scale is a times random scale. This means that if the maximum value on the scale were 5.0, then you would find that particular crystal orientation that corresponds to the peak 5 times more often than you would find the same crystal orientation in a completely randomly oriented sample. In order to get a more quantitative number, you would then have to integrate over the volume of the sample. In OIM, we achieve this by creating crystal orientation maps, where we manually enter the crystal direction we are interested in, and create maps that give a precise volume fraction of that particular orientation in the sample. We can choose the crystal directions based on the peaks we notice in the pole figures. For example, if we notice a peak of <111> crystal directions oriented in the transverse direction, we can map just these directions within a specific tolerance, and produce a map that gives the precise volume fraction present" [32].

Appendix B: Analysis of Variance for Autoclave Exposure Data

Analysis of variance answers the question whether conclusions drawn from data is statistically significant or whether the data can be explained by chance alone. Before delving into mathematical methods, descriptive statistics provides insight. The plots of capacitance against time in the body of this report include error bars to highlight the variability of the data. Since the autoclave experiments were collected with unequally sized data sets (capacitance measurements) at uneven time intervals, some statistical methods that may not be familiar to the reader must be used. The selection of the method and the calculations are briefly described.

Before selecting the statistical methods to study the analysis of variance for the data, the underlying distribution must be known. The distributions of figures are clearly normal by inspection. However, the sample distributions shown in figure 9 do not appear normally distributed. The Lilliefors test is used when the population mean and variance are unknown. Figure 20 is the plot of the Cumulative [Normal] Distribution Function (CDF) and the Sample Cumulative Distribution Function (SCDF) calculated in a spread sheet (not included). The decision criterion is based on comparing the greatest difference between the CDF and SCDF to a statistic [35]. In this case, the greatest difference (0.28) occurs when the standard normal variable equals 0.087. The test statistic is 0.11 at alpha equals 0.01, so the null hypothesis that the distribution is normal is rejected.
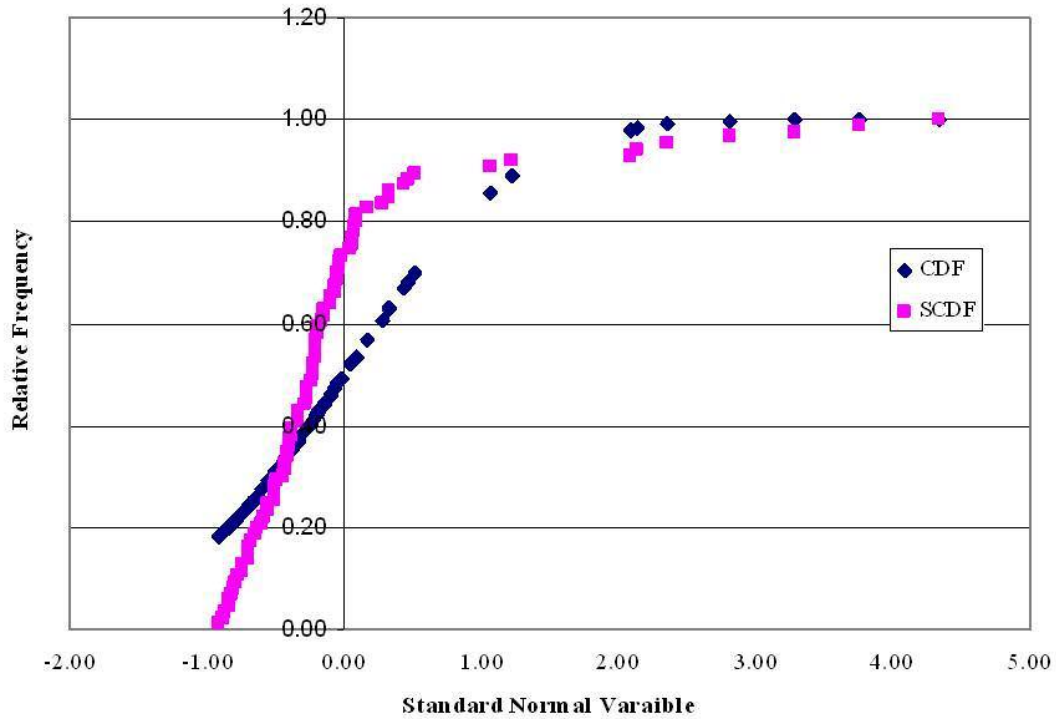
Figure 24: Initial Kemet BME - Lilliefors Test

Previous tables and graphs show that exposure to high humidity changes the average capacitance of MLCCs, and error bars showed symmetric distributions (that the mean was close to the center) at most time steps. The question remains whether or not exposure changes the population variance over time. One way of gaining confidence that there is only one aging process is showing that the variance is stationary through time and only the average value changes. Figure 24 shows the samples variances for the 0805 samples as a plot. All samples show some changes initially, typical of all measurements of ferroelectric capacitors [38] [39]. However, the measurements settle. Statisticians test for constant variance by showing what they call homogeneity of variance (also called homoscedasticity). There are sets of statistical methods used for homogeneity of variance, and the following description is from simplest (and least general) to complex (and most general). The F test (familiar from a first course in statistics) is used when two

variances from normal populations are compared. The F test is generalized as the Hartley test when there are more than two groups, still all normally distributed with a fixed sample size. If the groups also have different sample sizes, then Bartlett's test is used [37]. If the groups are also not normally distributed, then the Levene test is used [36]. Since the Murata BMNE and Kemet PME are both normal distributions with unequal sample sizes, Bartlett's test will be used for homogeneity of variance. The Levene test will be used for the non-normal Kemet BME homogeneity of variance test.
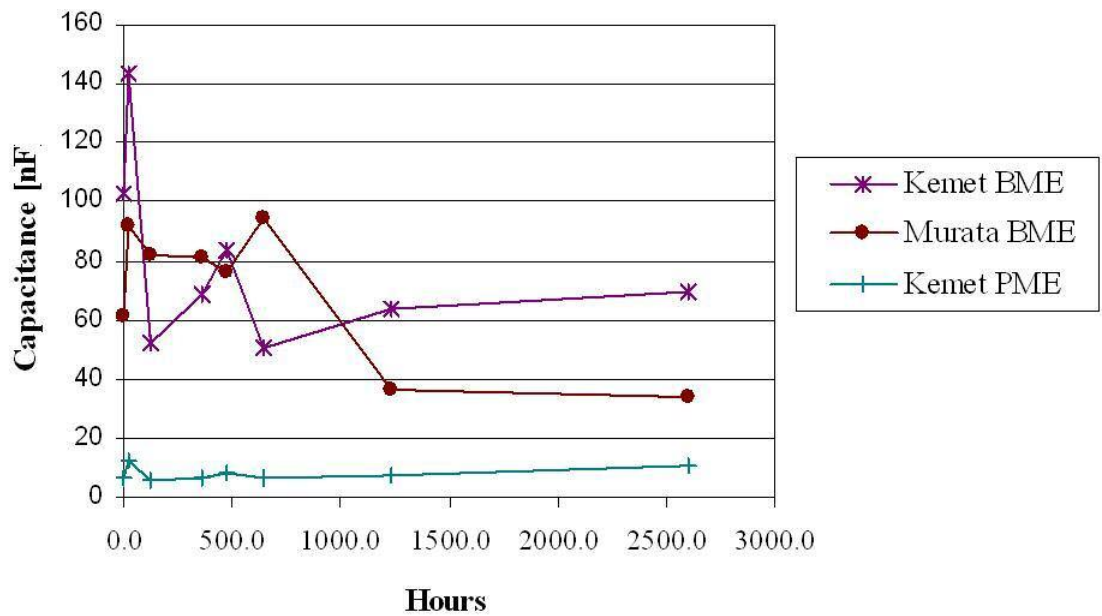
Figure 25: EIA 0805 Variances during Autoclave

Bartlett's test is based on the null hypothesis test that the variances of all k samples are equal. The alternative hypothesis is the negative.

$$H_o : \sigma_1^2 = \sigma_2^2 = ... = \sigma_k^2 \qquad (8)$$

Bartlett's test statistic is as follows where s is the pooled variance.

$$\chi^2 = \frac{\ln(10)\left[(\log s^2)\sum_{i=1}^{k}(n_i-1)-\sum(n_i-1)\log s_i^2\right]}{1+\left(\dfrac{1}{3(k-1)}\right)\left(\sum_{i=1}^{k}\dfrac{1}{n_i-1}-\dfrac{1}{\sum_{i=1}^{k}n_i-1}\right)} \qquad (9)$$

The null hypothesis will be rejected if

$$\chi^2 \geq \chi^2_{(1-\alpha)(k-1)} \qquad (10)$$
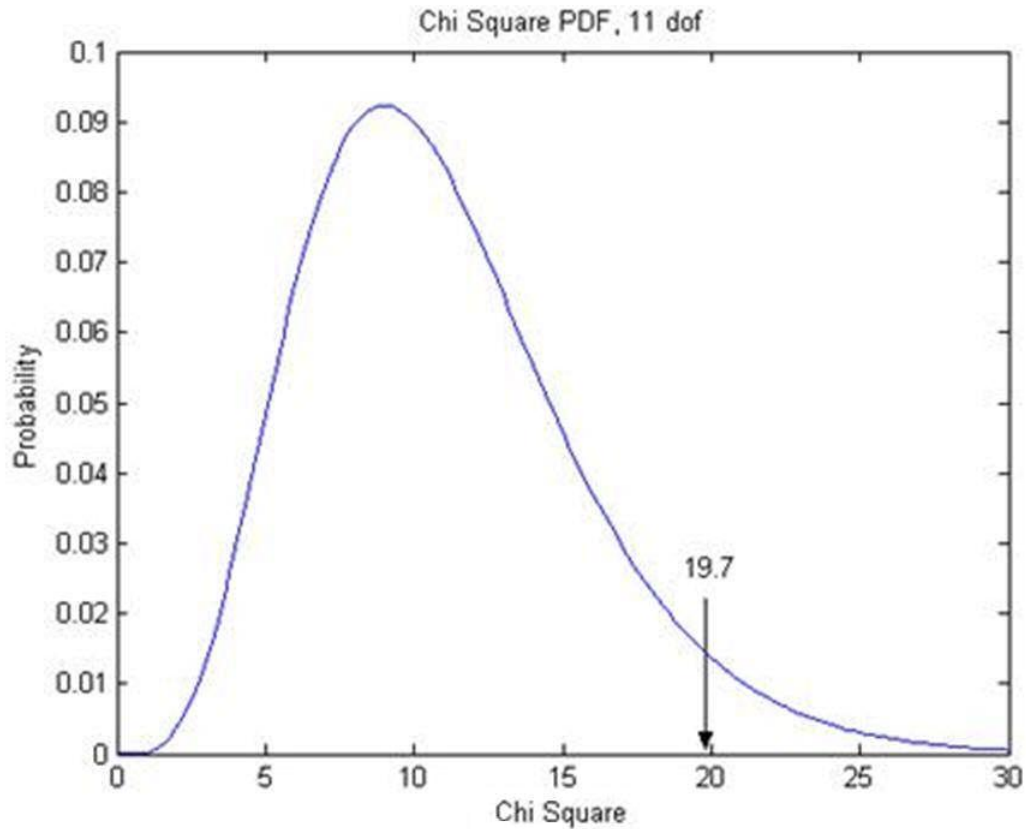
Figure 26: Bartlett's Test Summary

The following table shows the conclusion for Bartlett's tests for the two data sets.

Table 15: Bartlett's Test Summary

Capacitor	Test Statistic	χ^2 at 5% confidence	Decision
Murata BME	5.3	19.7	Accept
Kemet PME	0	19.7	Accept

The Levene test is less sensitive to departures from normality, and it will be applied to the Kemet PME data. The test statistic for the Levene test appears below. In this expression, the random variable X is of sample size N divided into k subgroups where N_i is the sample size of the ith subgroup. Z_{ij} is defined as the absolute value of the difference between each sample and the corresponding group mean. $\overline{Z}_i$ is the group mean, and $\overline{Z}..$ is the overall mean. [36] .

$$W = \frac{(N-k)\sum_{i=1}^{k} N_i (\overline{Z}_{i.} - \overline{Z}_{..})^2}{(k-1)\sum_{i=1}^{k}\sum_{j=1}^{N_i} (Z_{ij} - \overline{Z}_{i.})^2} \qquad Z_{ij} = \left| X_{ij} - \overline{X}_i \right| \qquad (11)$$

The null hypotheses (that the variances are equal) is rejected when $W > F_{(\alpha,k-1,N-k)}$. The following table summarizes the Levene test for the Kemet BMEs. However, this result does not negate the general trend. Furthermore, the results for later stages would yield different results. The trend in table shows that the variance reduced over time.

Table 16: Levene Test

Group	Sum Z_i	N_i	Group Means Zbar(i.)	$N_i*(Zbar(i.)-Xbar(..))^2$	
1	4000.1	86	46.51	5.65E+04	
2	2044.8	32	63.90	5.93E+04	
3	877.0	9	97.44	5.28E+04	
4	669.1	17	39.36	5.81E+03	
5	43.6	30	43.63	1.55E+04	
6	56.2	30	56.19	3.74E+04	
7	58.4	30	58.37	4.22E+04	
8	58.5	30	58.46	4.24E+04	
9	65.4	30	65.37	5.94E+04	
10	36.7	30	36.70	7.52E+03	
11	44.4	30	44.36	1.66E+04	
12	58.9	30	58.90	4.34E+04	
	8013	384		4.39E+05	
			Wnum=	1.63E+08	
Zbar(..)	20.87				
			Wnum=	1.84E+07	
			F=	1.81	5%
			W=	8.86	
			Reject Ho		

The initial capacitor samples were baked for over 100 hours. The following table summarizes the statistical test, Student's t test, of the difference between the initial against the dried samples. The null hypothesis is that the initial mean capacitance is equal to the dried mean capacitance. The conclusion is that the change in the mean due to drying is significant, not due to chance alone.

Table 17: Change due to Drying

	Initial Sample			147 Hours of Drying at 125 C			Test Statistics		Degrees Freedom	t at 0.05	Test Hypothesis
	n_i	$xbar_i$	s_i	n_i	$xbar_i$	n_i	s_p	t	dof	t	Outcome
Kemet BME	86	881	85	32	946	102.6	5.31	59.2	116	1.98	reject
Murata BME	106	1154	53.3	37	1246	61.2	40.5	119.1	141	1.98	reject
Kemet PME	100	94	6.7	24	106	6.6	1.43	36.8	122	1.98	reject

Appendix C: Generalized MLCC Manufacturing Methods

A generalized process flow for manufacturing BME MLCCs is described below, including important process changes in the process from manufacturing PME MLCCs. The patents by TDK [63] and Philips [64] provide the best description found in the literature, although other references include details of the manufacturing process [12] [75]. The box in figure 26 representing heat application steps is highlighted, because these are the process steps where oxygen vacancies are created. Table 18 further outlines the origin of the oxygen vacancy generating steps [16] [64] [76]. A lower temperature firing is required to prevent melting the electrode alloy when using low palladium content PME MLCCs (palladium content is typically less than 35% atomic). Air is used during firing of the PME MLCCs, but a reducing atmosphere is required when firing the BME MLCCs. A re-oxidizing step at 1000 ºC is added to the manufacturing of BME

Blending Powders → Heat Applications → Polishing

Wet Milling ← Dicing ← Add Terminations

Calcining ← Laminating ← MLCC Testing

Grinding ← Electrode Printing

Mixing into Paste → Tape Casting
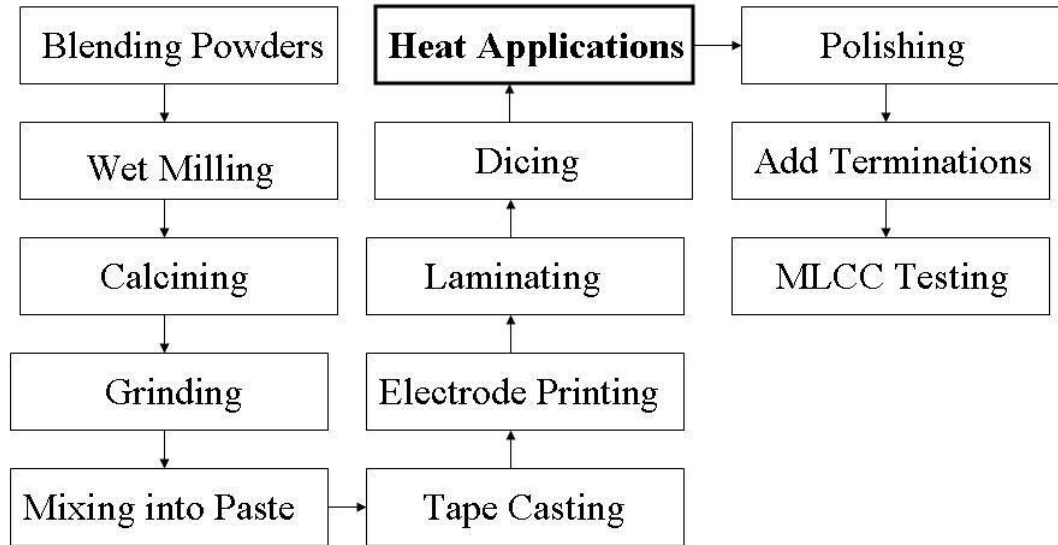
Figure 27: MLCC Manufacturing Process Steps

Table 18: Manufacturing Changes from PME to BME that Introduce Oxygen Vacancies

	Low Palladium Content PME Heating Atmosphere [16] [76] [80]	BME Heating Atmosphere [63]
Sintering	Air at approximately 1150 ℃ for silver-palladium with less than 35 atomic percent palladium	Humidified nitrogen and hydrogen with partial pressure of oxygen less than 10^{-8} atmospheres, 1350 ℃
Re-oxidation	Step not required	Humidified nitrogen and hydrogen with partial pressure of oxygen between 10^{-7} and 10^{-4} atmospheres, 1000 ℃

Appendix D: Ellingham Diagram Construction for MLCCs

BME MLCCs have nickel electrodes. Firing must avoid oxidizing nickel, and this requirement negates the easier practice of firing in air, the art for precious metal MLCCs. A reducing atmosphere must be used instead. The reducing atmosphere has the undesirable effect of reducing the barium titanate, thereby creating oxygen vacancies [51]. The Ellingham diagram is the standard method of providing a thermodynamic perspective for oxidation of metals. Since the oxidation – reduction (redox) issue is primary to this thesis, the Ellingham diagram is produced for the most important reactions in the firing of MLCCs in this appendix. The derivation will follow the development in the classic metallurgy text by Gaskell [40]. Thermodynamic constants for reactions will be taken from Binneweis and Milke [45]. Table 19 is a summary of the materials constants.

From the Ideal Gas Law where P is pressure, V is volume, R is the ideal gas constant (R = 8.314 Joules/mole) and T is temperature

$$PV = RT \tag{12}$$

And the definition of enthalpy where U is internal energy

$$H = U + PV \tag{13}$$

And the definitions of specific heats where C_v is the heat capacity at constant volume and C_p is the heat capacity at constant pressure

$$C_v = \left(\frac{\partial U}{\partial T} \right)_v \tag{14}$$

$$C_p = \left(\frac{\partial H}{\partial T}\right)_p \qquad (15)$$

The difference between the two specific heats is:

$$c_p - c_v = \left(\frac{\partial V}{\partial T}\right)_P \left[P + \left(\frac{\partial U}{\partial V}\right)_T\right] \qquad (16)$$

Which for an ideal gas becomes:

$$c_p - c_v = R \qquad (17)$$

Experimental data for specific heats is represented in the form:

$$c_p \cong a + bT + cT^{-2} \qquad (18)$$

The 1st Law of Thermodynamics (deltas implying path dependence)

$$dU = \delta q - \delta w \qquad (19)$$

Combining with the 2nd Law of Thermodynamics (for a closed, reversible process)

$$dU = TdS - PdV \qquad (20)$$

Helmholtz free energy:

$$A = U - TS \qquad (21)$$

Gibbs free energy:

$$G = U + PV - TS = H - TS \qquad (22)$$

The Gibbs Free Energy is a key important concept underpinning the Ellingham Diagram, and it is articulated in the book by Barrett (and his coauthors) while at Stanford, Barrett is the former Chief Executive Officer of Intel Corporation: "In our description of chemical equilibrium we pointed out that the equilibrium involves consideration of both the energy of a system and the tendency for mixing. ... At equilibrium the internal energy tends to assume a minimum value, while the entropy and mixing energy tend to seek a maximum

value. …we must be careful to say that it is the free energy that seeks a minimum value. …the approach to equilibrium is accompanied by either an increase in the internal energy or a decrease in the entropy"[33].

Extending the previous ideas as differentials

$$dH = TdS + VdP \tag{23}$$

$$dA = -SdT - PdV \tag{24}$$

$$dG = -SdT + VdP \tag{25}$$

Extending to changing species represented as subscripts i

$$dG = -SdT + VdP + \sum_{i=1}^{i=k} \left(\frac{\partial G}{\partial n_i} \right)_{T,P,n_j,\dots} dn_i \tag{26}$$

With the definition of μ_i for the chemical potential of species i where the chemical potential of the species i in a phase is a measure of the tendency of the species i to leave the phase, then

$$dG = -SdT + VdP + \sum_{1}^{k} \mu_i dn_i \tag{27}$$

For constant T & P, integrating for a system of n moles:

$$G' = \sum_{i} \mu_i n_i \tag{28}$$

For closed systems, fixed composition, constant pressure provides the Gibbs-Helmholtz Equation

$$\frac{d(\Delta G/T)}{dT} = -\frac{\Delta H}{T^2} \tag{29}$$

$$\Delta H = H(T_2, P) - H(T_1, P) = \int_{T_1}^{T_2} c_p dT \tag{30}$$

85

Introducing the notation $\quad \Delta c_p = c_{P_{A(l)}} - c_{P_{A(s)}}$ (31)

$$\Delta H_{T2} = \Delta H_{T1} + \int_{T1}^{T2} \Delta c_p dT$$ (31)

The phase equilibria in one component system:

$$G_{(l)} = G_{(s)} \quad \text{or} \quad dG_{(l)} = dG_{(s)}$$ (32)

The Clapeyron Equation

$$\left(\frac{dP}{dT}\right)_{eq} = \frac{\Delta H}{T\Delta\Delta}$$ (33)

with

$$\Delta V = V_{vapor} \equiv V_v$$ (34)

and the ideal gas law,

$$\frac{dP}{P} = \frac{\Delta H}{RT^2} dT$$ (35)

The Clausius-Clapeyron Equation

$$d(\ln P) = \frac{\Delta H}{RT^2} dT$$ (36)

Considering a reaction at constant temperature and pressure in a chemical formula like A + B -> 2C:

$$G' = n_A \overline{G}_A + n_B \overline{G}_B + n_C \overline{G}_C = n_i \sum \overline{G}_i$$ (37)

ΔG^o is the standard free energy change for the chemical reaction at T; the difference between the sum of the free energies of the reaction products in their standard states and the sum of the free energies of the reactants in their standard states.

$$G^o = -RT \ln\left(\frac{p_C^2}{p_A p_B}\right) = -RT \ln\left(\frac{X_C^2}{X_A X_B}\right) \tag{38}$$

The units of G^o are $\dfrac{\text{Joules}}{\text{gmole}}$.

Defining the equilibrium constant,

$$K = \left(\frac{p_C^2}{p_A p_B}\right) \tag{39}$$

$$\Delta G^o = -RT \ln K \tag{40}$$

where $K = \ln\left(\dfrac{1}{p_{O_2}}\right)$ …depending upon the coefficient in the reaction balance

$$\Delta G_T^o = \Delta H_T^o - T\Delta S_T^o = \Delta H_{298}^o + \int_{298}^{T} \Delta c_p \, dT - T\Delta S_{298}^o - T\int_{298}^{T} \frac{\Delta c_p}{T} dT \tag{41}$$

Using c_p from above

$$\left(\frac{\partial \Delta H^o}{\partial T}\right)_P = \Delta c_p = \Delta a + \Delta bT + \Delta cT^{-2} \tag{42}$$

Integrating yields

$$\Delta H_T^o = \Delta H_o + \Delta aT + \frac{\Delta bT^2}{2} - \frac{\Delta c}{T} \tag{43}$$

$$\Delta G_o = CT + \Delta H_o - \Delta aT \ln T - \frac{\Delta bT^2}{2} - \frac{\Delta c}{2T} \tag{44}$$

$$\ln K = \frac{-H_o}{RT} - \frac{C}{R} + \frac{\Delta a \ln T}{R} + \frac{\Delta bT}{2R} + \frac{\Delta c}{2RT^2} \tag{45}$$

Finally we get to the utilitarian expression by Effingham from 1944

$$\frac{\Delta G^{\circ}}{RT} = -\ln\left(p^{-1}\right) \qquad (46)$$

Recalling that

$$\ln(x) = \ln(10)\log(x) \qquad (47)$$

Table 19: Thermodynamic Data for Ellingham Diagram

Element or Compound	Melting Point [K]	ΔH [kJ/mole]	S_{298} [kJ/mole]	c_p [J/molK]			
				a	$b\ (10^{-3})$	$c\ (10^6)$	$d\ (10^{-6})$
Ba	1002	0	62.4	13.26	52.32	0	0
Ca	1115	0	41.6	16.38	22.11	0.26	0
O_2	55	0	205.1	29.15	6.48	-0.18	-1.02
Ni	1728	0	29.9	19.36	22.46	0.02	0
Sr	1050	0	55.7	22.22	13.89	0	0
Ti	1939	0	30.8	22.24	10.21	-0.01	0
NiO	2228	-239.7	38	-6.32	131.24	1.02	0
SrO	2938	-592	55.5	50.75	6.07	-0.63	0
TiO	2023	-542.7	34.8	44.22	15.06	-0.78	0
CaO_2	-	-659	8307				
$TiO_{2\ (rutile)}$	2130	-944.7	50.6	73.35	3.05	-1.7	0
NiO_3	1538	-66.5	53.1	53.01	9.62	-0.81	0
Ti_2O_3	2115	-1520.9	77.3	53.07	163.44	0	0
$NiTiO_3$	-	-1201.4	82.6	115.1	15.98	-1.83	0
$BaTiO_3$	1988	-1647.7	110.2	121.46	8.54	-1.82	0

Using a spreadsheet with the relations described above and the constants in table 19
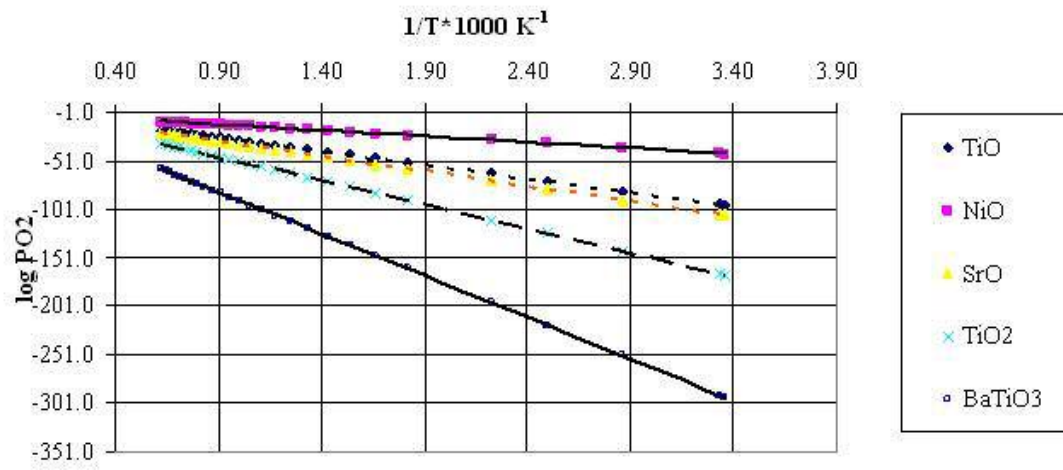
generated the following figure.

Figure 28: Ellingham Diagram for BME MLCC Firing

References:

[1] JEDEC Solid State Technology Association, Accelerated Moisture Resistance – Unbiased HAST, JESD22-A102-C, Arlington, VA, Dec. 2000.

[2] Electronic Industries Association, Ceramic Dielectric Capacitors Classes I, II, II and IV, Part II: Test Methods, Revision E, EIA-198-2, Arlington, VA, January 1998.

[3] International Electrotechnical Commission, Basic Environmental Testing Procedures Part 2: Tests - Test CA: Damp Heat, Steady State, Revision 69, IEC 60068-2-3, Geneva, Switzerland, 1984.

[4] International Electrotechnical Commission, Semiconductor Devices – Mechanical and Climatic Test Methods - Part 33: Accelerated Moisture Resistance - Unbiased Autoclave, Revision 4, IEC 60749-33, Geneva, Switzerland, 2004.

[5] Donahoe, D., Hillman, C., Pecht, M., Failures in Base Metal Electrode Capacitors, 23rd Capacitor and Resistor Technical Symposium, March 31-April 3, 2003, pp. 129-133.

[6] Brusse, J., Sampson, M., COTS Ceramic Chip Capacitors: An Evaluation of the Parts and Assurance Methodologies, 24th Capacitor and Resistor Technical Symposium, March 29-April 1, 2004, pp. 128-140.

[7] Randall, M., Gurav, A., Skamser, D., Beeson, J., Lifetime Modeling of Sub 2 Micron Dielectric Thickness BME MLCC, 23rd Capacitor and Resistor Technical Symposium, March 31-April 3, 2003, pp. 134-140.

[8] Paulsen, L., Reed, E., Highly Accelerated Lifetesting of Base-Metal-Electrode Ceramic Chip Capacitors, Microelectronics Reliability, Volume 42, 2002, pp. 815-820.

[9] Prokopowicz, T., Vaskas, A., Final Report, Research and Development Intrinsic Reliability Subminiature Ceramic Capacitors, ECOM Report 90705-F, NTIS AD-864068, October 1969.

[10]   Saff, E. and Snider, A., Fundamentals of Complex Analysis, Third Edition, Prentice Hall, Upper Saddle River, NJ, 2003, p. 8.

[11]   Brandt, R., Ansel, G., Aging in Tetragonal Ferroelectric Barium Titanate, Journal of the American Ceramic Society, Vol. 52, No. 4, April 1969, pp.192-199.

[12]   Kahn, M., Burks, D., Burn, I., Schulze, Ceramic Capacitor Technology, in Levinson, L. [Ed], Electronic Ceramics, Marcel Decker, NY, 1988, pp. 191-274.

[13]   Maloy, S., What is the Capacitance of this Capacitor?, TDK Components USA, Inc, June 1999.

[14] Ochi, A., Saito, S., Utsumi, K., Yonezawa, M., Small Y5V Chip-Capacitors with Very Large Capacitance, Electronics Components Conference, 1988, Proceedings of the 38th, 9-11 May 1988, pp 95 –100.

[15] Welder, G., Klemperer, D., Chemisorption: An Experimental Approach, Butterworths, London, 1976, p. 1.

[16] Burn, I., Ceramic Capacitor Dielectrics, in Schneider, S. [Ed], Engineered Materials Handbook, Volume 4, Ceramics and Glasses, ASTM, 1991, pp. 1112-1118.

[17] Kolasinski, K., Surface Science, John Wiley and Sons, New York, 2002, p. 85.

[18] Mason, Aging Properties of Barium Titanate and Related Ferroelectric Ceramics, The Journal of the Acoustical Society of America, Volume 27, Number 1, January 1955, pp. 73-85.

[19] Hebert, J., Production of Ceramic Material, U.S. Patent 3,041,189, 26 June 1962.

[20] Park, Y., Kim, Y. and Kim, H., The Effect of Stress on the Dielectric-Temperature Characteristics of Core-Shell Grain Structure, J. Phys. D: Appl. Phys. 29 (1996), pp. 2483-2491.

[21]   Kiriyama, S., Monolithic Ceramic Capacitors Help Reduce Noise in Personal Computers, Asia Electronics Industry, March 2003, http://www.murata.com/articles/ta02a4.pdf (15 September 2004), pp. 46-49.

[22]   Nakano, Y., Nomura, T., Takenaka, T., Residual Stress of Multilayer Ceramic Capacitors with Ni-Electrodes, Japanese Journal of Applied Physics, Vol. 4, No. 9B, September 2003, pp. 6041-6044.

[23]   Nesbitt, H., Bancroft, G., Fyfe, W., Karkhanis, S., Nishijima, A., Shin, S., Thermodynamic Stability and Kinetics of Perovskite Dissolution, Nature, Vol. 289, 29 January 1981, pp. 358-362.

[24]   Kao, K., Dielectric Phenomena in Solids, Elsevier Academic Press, Amsterdam, 2004, pp. 221-225.

[25]   Utech, B., The Effect of Solution Chemistry on Barium Titanate Ceramics, M.S. Thesis, Pennsylvania State University, May 1990, pp. 25-63.

[26]   Haertling, G., Ferroelectric Ceramics: History and Technology, Journal of the American Ceramic Society, Vol. 82, No. 4, April 1999, pp. 797-818.

[27]   Smith, L., Decoupling Capacitor Calculations for CMOS Circuits, IEEE 3rd Topical Meeting Electrical Performance of Electronics Packaging, 2-4 Nov. 1994, pp. 101-105.

[28]   Macdonald, J., Impedance Spectroscopy, John Wiley and Sons, NY, 1987, pp. 4-11.

[29]   Hennings, D., Schreinemacher, H, Wagemans, H., U.S. Patent 5841625, Ceramic Multilayer Capacitor, 24 Nov. 1998.

[30]   Ward, P., Some Observations on Recent MLCs Quality as Experienced in Europe, Including Discussion of Two Types of DPA Analysis, undated, http://www.avc.com (16 May 2003).

[31]   Schwartz, A., Kumar, M., Adams, B., Electron Backscatter Diffraction in Materials Science, Kluwer Academic, New York, 2000, pp. 1-2.

[32]   Email, Witt, R., Times Random Scale, 2 Sept. 2004.

[33]   Barrett, C., Nix, W., Tetelman, A., The Principles of Engineering Materials, Prentice-Hall, Englewood Cliffs, NJ, 1973.

[34]   Randle, V., Microtexture Determination and its Applications, 2nd Ed., Maney, London, 2003, pp. 77-87.

[35]   Pfaffenberger, R. and Patterson, J., Statistical Methods for Business and Economics, 3rd Ed., Irwin, Homewood, IL, 1987, pp. 1030-1032.

[36] NIST, Levene Test for Equality of Variances, http://www.itl.nist.gov/898/handbook.eda/section3/eda.html (26 June 2004).

[37] Ostle, B. and Mensing, R., Statistics in Research, 3rd Ed., Iowa State Press, Ames, 1975, pp. 127-129.

[38] Lines, M. and Glass, A., Principles and Applications of Ferroelectrics and Related Materials, Clarendon Press, Oxford, 1977, p.111-112.

[39] Arlt, G., Twinning in Ferroelectric and Ferroelastic Ceramics: Stress Relief, Journal of Materials Science, Vol;. 25, 1990, pp. 2655-2666.

[40] Gaskell, D., Introduction to Metallurgical Thermodynamics, McGraw-Hill, NY, 1973, pp. 8-250.

[41] NIST Scientific and Technical Databases, NIST X-ray Photoelectron Spectroscopy Database, 16 Dec. 2003, http://www.srdata.nist.gov/xps/index.htm (19 Nov. 2004).

[42] Moore, J. and Spencer, N., Encyclopedia of Chemical Physics and Physical Chemistry, Volume II: Methods, Institute of Physics Publishing, Philadelphia, 2001.

[43] Department of Chemistry and Biochemistry, Instrumentation, http://www.chem.umd.edu facility/xps.html (20 Nov. 2004).

[44]   Chaing, Y., Birnie, D., Kingerly, W., Physical Ceramics, John Wiley and Sons, New York, 1997, pp. 47-49.

[45]   Binneweis, M and Milke, E., Thermochemcial Data of Elements and Compounds, Wiley-VCH, 1999, pp. 127-885.

[46]   Randall, C., Newnham, R., Cross, L., History of the First Ferroelectric Oxide, BaTiO$_3$,   http://www.209115.31.62/electronics division/History%of%20Barium%20Titanate.pdf (26 September 2004).

[47]   Donahoe, D. and Ganesan, S., Method to Sort Capacitors by Type, U.S. Provisional Patent Application, PS-2004-028, University of Maryland Office of Technology Commercialization, 30 March 2004.

[48]   McCammon, C., Becerro, A., Lauterbach, S., Blass, U., Marion, S., Langenhorst, R., Aken, P., Siefert, F., Oxygen Vacancies in Perovskite and Related Structures: Implications for the Lower Mantle, Material Research Society Symposium Proceedings, Volume 718, 2002, pp. D2.3.1 - D2.3.6.

[49]   BME MLCCs: Dielectrics in Motion, Passive Component Industry, November/December, 1999, pp. 8-11.

[50]   Chin, S., Palladium Prices Top $1000 per Ounce, EBN, 15 January, 2002, http://www.ebnonline.com (18 October 2002).

[51]   Sakabe, Y. and Reynolds, T., Bas-Metal Electrode Capacitors, American Ceramic Society Bulletin, Volume 81, Number 10, October 2002, pp. 24-26.

[52]   Kishi, H., Mizuno, Y. and Chazono, H., Base Metal Electrode Multilayer Ceramic Capacitors: Past, Present and Future Perspectives, Japanese Journal of Applied Physics, Volume 42, Number 8, July 2003, pp. 4-19.

[53]   Zhang, W. and Malanga, D., Copper End Terminations for BME Capacitors, 1 June 2001, http://www.ceramicindustry.com (20 May 2004).

[54]   Leygraph, C. and Grandtl, T., Atmospheric Corrosion, Wiley-Interscience, New York, 2000, p. 294.

[55]   ASTM F 97-72 Standard Practice for Determining Hermiticity of Electron Devices by Dye Penetration and E 165 Practice for Liquid Penetrant Testing

[56]   Anderson, J., Brady, G., Merz, W., Remeika, J., Effects of Ambient Atmosphere on the Stability of Barium Titanate, Journal of Applied Physics, Vol. 26, No. 11, 1955, pp. 1387-1388.

[57]   Mason, W., Aging of the Properties of Barium Titanate and Related Ferroelectric Ceramics, The Journal of the Acoustic Society of America, Vol. 27, No. 1, Jan. 1955, pp. 73-85.

[58]   Siegel, E. and Muller, K, Local Position of Fe^{3+} in Ferroelectric $BaTiO_3$, Physical Review B, Vol. 20, No. 9, 1 Nov. 1979, pp. 3587-3596.

[59]   Nesbitt, H., Bancroft, G., Fyfe, W., Karkhanis, S., Nishijima, A., Shin, S., Thermodynamic Stability and Kinetics of Perovskite Dissolution, Nature, Vol. 289, 29 Jan. 1981, pp. 358-362.

[60]   Yoo, I., Burton, L., Stephenson, F., Electrical Conduction Mechanisms of Barium Titanate Based Thick Film Capacitors, IEEE Trans. On Components, Hybrids and Manufacturing Technology, Vol. CHMT-10, No. 2, June 1987, pp. 274-282.

[61]   Herbert, J. and Best, P., Method of Applying a Metal Electrode to a High Permittivity Ceramic, United States Patent 2,750,657, 19 June 1956.

[62]   Zogbi, D., Product Development Trends in Capacitors During 2003, TTI, Inc., 10 Dec. 2004, http://www.ttiinc.com, (28 Nov. 2004).

[63]   Nomura, T., Nakano, Y., Satoh, A., Hitomi, A., Multilayer Ceramic Capacitor, United States Patent 5,319,517, 7 June 1994.

[64]   Hennings, D. and Schreinemacher, Multilayer Ceramic Multilayer Capacitor, United States Patent 5,841,625, 24 Nov. 1998.

[65]   Cross, L. and Newnham, R., History of Ferroelectrics, Ceramics and Civilization, Volume III, High Technology Ceramics – Past, Present and Future, The American Ceramics Society, 1087, pp. 289-301.

[66]   Kwei, G., Lawson, A., Billinge, S., Cheong, S., Structures of Ferroelectric Phases of Barium Titanate, Journal of Physical Chemistry, Vol. 97, 1993, pp. 2368, 2377.

[67]   Nomura, T., Miura, T., Arashi, T., Nakano, Y. and Sato, A., Multilayer Ceramic Capacitors – Recent Trends, Proceedings of the Tenth IEEE International Suppliers Symposium on Applications of Ferroelectrics, Aug. 1996, pp. 135-141.

[68]   Moulson, A. and Hebert, J., Electroceramics, 2nd Ed., John Wiley and Sons, West Sussex, England, 2003, pp. 75-77.

[69]   Zhang, X., Hashimoto, T. and Joy, D., Electron Holographic Study of Ferroelectric Domain Walls, Applied Physics Letters, Vol. 60, No., 6, 10 Feb. 1992, pp. 784-786.

[70]   Cheng, B., Gabbay, M, Fantozzi, G., Anelastic Relaxation Associated with the Motion of Domain Walls in Barium Titanate Ceramics, Journal of Materials Science, Vol. 31, 1996, pp. 4141-4147.

[71]   Mitoseriu, L., Harnagea, C., Nanni, P., Testino, A., Zhao, Z., Nygren, M., Local Switching Properties of Dense Nanocrystalline BaTiO$_3$ Ceramics, Applied Physics Letters, Vol. 84, No. 13, 29 March 2004, pp. 2418-2420.

[72]   Warren, W., Dimos, D., Tuttle, B., Electronic and Ionic Trapping at Domain Walls in BaTiO$_3$, Communications of the American Ceramic Society, Vol. 77, No. 10, 1994, pp. 2753-2757.

[73]   Scott J. and Dawber, M., Oxygen Vacancy Ordering as a Fatigue Mechanism in Perovskite Ferroelectrics, Applied Physics Letters, Vol. 76, No. 25, 19 June 2000, pp. 3801-3803.

[74]   Welder, op. cit., p. 36.

[75]   Utech, op. cit., p. 20.

[76]   McSweeney, R. and Long, S., Low Fire Ceramic Dielectric Composition for Multilayer Ceramic Capacitors, U.S. Patent 4499522, 12 Feb. 1985.

[77]   Chiang, op. cit., p. 117.

[78]   Barsoum, M., Fundamentals of Ceramics, Chapter 10: Sintering and Grain Growth, McGraw-Hill, NY, 1997, pp. 331-390.

[79]   Ling, H. and Jackson, A., Correlation of Silver Migration with Temperature-Humidity-Bias (THB) Failures in Multilayer Ceramic Capacitors, IEEE Transactions on Components, Hybrids and Manufacturing Technology, Vol. 12, No. 1, March 1989, pp. 130-137.

[80]   Tazamizawa, H., Utsumi, K., Yonezawa, M., Ohno, T., Large Capacitance Multilayer Ceramic Capacitor, IEEE Transactions on Components, Hybrids and Manufacturing Technology, Vol. CHMT-4, No. 4, Dec. 1981, pp. 345-349.

[81]   ASTM International, Standard Test Method for Liquid Penetrant Examination, E 165-02, Annual Book of ASTM Standards 2004, West Conshohocken, PA, pp. 61-68.

[82]   Hoelscher, R., Springer, C., Dobrovolny, Graphics for Engineers, John Wiley and Sons, New York, 1968, p. 12.

[83]   Grob, B., Basic Electronics, Fifth Edition, McGraw-Hill, New York, 1984, p. 557.

[84]   Paul, C., Introduction to Electromagnetic Compatibility, John Wiley and Sons, New York, 1992, 744-749.